F-ANG+: A 3-D Augmented-Stencil Face-Averaged Nodal-Gradient Cell-Centered Finite-Volume Method for Hypersonic Flows

Jeffery A. White[1]
NASA Langley Research Center, Hampton, VA, 23681, USA
Hioraki Nishikawa[2]
National Institute of Aerospace, Hampton, VA, 23666, USA
Matthew D. O'Connell[3]
NASA Langley Research Center, Hampton, VA, 23681, USA

We describe the extension of a 2-D simplified face-averaged nodal-gradient (F-ANG) method to 3-D and demonstrate that the 3-D simplified F-ANG method is accomplished by augmenting the node-centered gradient least squares stencil. This augmented stencil F-ANG method is shown to result in advection and diffusion schemes that are stable for hexahedral, prismatic, pyramidal and tetrahedral cells without having to resort to cell-averaged nodal gradients. In addition, we describe the modifications to the augmented stencil required to support the use of wall function boundary conditions. Finally, we describe a consistent, cell-based multidimensional limiter procedure (MLP), and show it to be fully consistent with the linearity-preserving unstructured-MUSCL (LP-U-MUSCL) scheme for all values of kappa. These methods and schema are implemented in the cell-centered finite-volume code VULCAN-CFD, which is then used to demonstrate the computation of 3-D hypersonic canonical problems using tetrahedral and mixed element grids as well as highly adapted tetrahedral grids.

1. Introduction

Commercial off-the-shelf (COTS) unstructured grid-generation tools have become widely used by the aerospace industry. These tools employ a wide variety of techniques to generate unstructured grids. The techniques can be divided into three categories; 1) prismatic cell layers near the wall blended with tetrahedral cells away from the wall, 2) prismatic and/or hexahedral cell layers near the wall blended with hexahedral cells away from the wall and 3) polygonal layers of cells near the wall blended with polyhedral cells away from the wall. All of these approaches require that flow solvers support multiple cell types. While unstructured grid generation using these approaches has matured and is becoming more automated, these tools can still produce grids containing problematic cells. Recent experience has shown that nonconvex cells and sliver cells are sometimes encountered (usually near boundaries) that can adversely or catastrophically affect flow-solver stability and convergence. Recently, a noncommercial approach to adaptive grid generation referred to as sketch-to-solution or S2S [1] has arisen where a coarse tetrahedral grid is initially generated on a computational domain defined by the user and a final grid is arrived at by repeatedly adapting the grid to the solution using feature-based or adjoint-based adaptation using the ***refine*** code [2] until some stopping criteria based on the convergence of engineering figures of merit is reached. When this approach is applied to hypersonic flows, the resulting adapted tetrahedral grids will contain high aspect ratio highly skewed tetrahedral cells near walls and shocks. These high aspect ratio highly skewed cells can make obtaining a solution quite difficult, even when using strong solvers such as JFNK [3]. Experience has shown that the least-squares gradients used to compute the fluxes and source terms are significant sources of the numerical difficulties encountered on these types of grids, and that careful attention to the location, formulation, and use of these gradients is crucial to developing a robust unstructured-grid flow solver.

Toward that end, over the past several years we have investigated several cell-centered [4-7] and node-centered [8-10] least-squares gradient methods. This effort led to the relatively recent development of a face-averaged nodal-gradient approach (F-ANG) that has performed well on pure tetrahedral grids [9], that was successfully extended to include nontetrahedral cells by combining F-ANG with cell-averaged nodal-gradients (C-ANG) to yield the face and cell-averaged nodal-gradient method (FAC-ANG) of Ref. [9]. Even more recently, a face-neighbor augmented stencil F-ANG method [11] was developed and tested in 2-D that demonstrated improved stability and robustness on problematic test grids that previously developed methods [4-10] were unable to achieve solutions on. This F-ANG+*fn* method also allows the F-ANG approach to be applied to all cell topologies without having to resort to the use of C-ANG for non-tetrahedral cells. The key feature of the F-ANG+*fn* method is the augmentation of the node-centered gradient stencils with additional face-neighbor and/or node-neighbor cells. The purpose of this paper is to 1) extend the 2-D method described in Ref. [11] to 3-D, 2) to show that it is stable for tetrahedral and nontetrahedral grids, 3) to investigate its

[1]Aerospace Technologist, (jeffery.a.white@nasa.gov), Computational AeroSciences Branch, MS 128, Associate Fellow, AIAA.
[2]Research Fellow, (hiro@nianet.org), 100 Exploration Way, Hampton, VA 23666 USA, Associate Fellow, AIAA.
[3]Aerospace Technologist, (matthew.d.oconnell@nasa.gov), Computational AeroSciences Branch, MS 128, Member, AIAA.

numerical properties on difficult/challenging grids using laminar and turbulent hypersonic flows, and 4) to demonstrate a new cell-based multidimensional limiter procedure (MLP) based on the approach of Park and Kim [12] that is fully consistent with the linearity-preserving unstructured-MUSCL (LP-U-MUSCL) version [13] of Burg's U-MUSCL scheme [14], for all values of kappa.

II. Methodology

A. Role, Importance and Construction of the Gradient.

Solution gradients are perhaps the most important and one of the most difficult quantities to obtain accurately and robustly on irregular, unstructured grids. The solution gradients are required to accomplish three things when computing the residual of the discrete equations for each time step/cycle of the solution process: 1) to perform the higher-order reconstruction when computing the inviscid fluxes, 2) to compute the cell-face gradient when computing the viscous fluxes, and 3) to compute the source terms for the turbulence modeling transport equations. Moreover, there is evidence in the literature that a different definition of the cell-average gradient may be required to compute each of these quantities [15].

While no single gradient method has been found to be accurate for all arbitrary polygons, with some caveats [16], the weighted least-squares (WLSQ) method has proven to be the preferred method [11,12] for node-centered and cell-centered 2nd-order finite-volume schemes. The WLSQ gradient method is based on a polynomial fit over a set of nearby data. For 2nd-order finite-volume schemes, the gradients need to be at least 1st-order accurate on general unstructured grids; and thus, it is sufficient to fit a linear polynomial. For a 2nd-order cell-centered finite-volume scheme, the authors are aware of at least three distinct ways to compute the gradients. These are to 1) compute the cell-centered gradient (CCG) directly using a cell-centered linear WLSQ method [4-7], 2) compute the node-centered (also known as the nodal gradients (NG)) using a node-centered linear WLSQ method [8-10,20-22] and then utilize some form of nodal- gradient averaging to compute the averaged nodal gradients (ANG) at the cell centroid [20-22] and/or the cell-face centroids [8-10] or 3) interpolate the cell-average solution to the nodes using a clipped pseudo-Laplacian interpolation and then compute the cell-centered gradient using Green-Gauss [23]. Of the three methods, we initially chose to concentrate our efforts on CCG, however, more recently our focus has been on face-averaged variants of the ANG-WLSQ gradient family of methods.

When faced with the need to construct gradients on unstructured hybrid grids, the methodology used to construct the fluxes at the faces of the control volume directly influence how one chooses to construct the gradients. Therefore, a review of the inviscid and viscous flux construction for a 2-D hybrid grid cell face, shown in red in Fig. 1 follows.

B. Role of the Gradient in Inviscid Flux Construction

If the inviscid fluxes are computed using an upwind flux scheme, a reconstruction-based 2nd-order finite-volume cell-centered scheme that utilizes an approximate Riemann solver such as the LDFSS [24] or HLLC schemes [25], requires that the inviscid flux reconstruction variables, q_i, (where i indicates inviscid state variables), be reconstructed at the left (L) and right (R) sides of the cell-face centroid, **X**, as shown in Fig. 2-a. The inviscid flux reconstruction variables are the cell-average variables defined as

$$q_i = \left(\frac{\rho_1}{\rho},\ldots,\frac{\rho_{ncs}}{\rho},\rho,u,v,w,P,k,\omega\right) \quad \text{for thermal equilibrium, or,}$$

$$q_i = \left(\frac{\rho_1}{\rho},\ldots,\frac{\rho_{ncs}}{\rho},\rho,u,v,w,T_{ve},P,k,\omega\right) \quad \text{for thermal nonequilibrium,}$$

where $\frac{\rho_1}{\rho},\ldots,\frac{\rho_{ncs}}{\rho},\rho,u,v,w,T_{ve},P,k,\omega$ are the chemical species mass fractions, from 1 to the number of chemical species, static density, Cartesian velocity components, vibrational/electronic temperature, static pressure, turbulent kinetic energy, and specific turbulent dissipation rate, respectively. A 1st-order accurate scheme results when the cell-average values, q_{ik}, of the cell to the left, k_L, and the cell to the right, k_R, of the cell face are used. A 2nd-order accurate scheme results when the L and R primitive variables are reconstructed to the cell face midpoint with an extrapolation method based on the left and right cell-average primitive variables and cell averaged or cell-face averaged inviscid gradients, q_{ik_L}, q_{ik_R}, and $\overline{\nabla q_i}^L, \overline{\nabla q_i}^R$, respectively, as given by

$$q_{if}^L = q_{ik_L} + \overline{\nabla q_i}^L \cdot \vec{r}_{Lf}, \tag{1}$$

$$q_{if}^R = q_{ik_R} + \overline{\nabla q_i}^R \cdot \vec{r}_{Rf}, \tag{2}$$

where $\vec{r}_{Lf}$ and $\vec{r}_{Rf}$ are vectors in Cartesian space drawn from the left and right cell centroids to the cell face centroid, respectively, as shown in Fig. 2-b. In addition to the scheme above, which is an unstructured-grid interpretation of Fromm's scheme [26], it is tempting to naively implement the higher-order unstructured-MUSCL (U-MUSCL) reconstruction scheme of Burg [14], which is written as

$$q_{if}^{L} = q_{ik_L} + \frac{\chi}{2}(q_{ik_R} - q_{ik_L}) + (1-\chi)(\overline{\nabla q}_i^{L} \cdot \vec{r}_{Lf}), \quad (3)$$

$$q_{if}^{R} = q_{ik_R} + \frac{\chi}{2}(q_{ik_L} - q_{ik_R}) + (1-\chi)(\overline{\nabla q}_i^{R} \cdot \vec{r}_{Rf}), \quad (4)$$

where χ is used to control the behavior and the 1-D order of accuracy of the scheme when the flow is smooth:

χ = 0, gives Fromm's scheme, gives a 2nd-order scheme,
χ = -1, gives a 2nd-order fully upwind scheme,
χ = 1/3, gives a 3rd-order upwind biased scheme.

However, Eqs. (3,4) were designed for edge-based schemes utilizing a median dual that explicitly assumes that the cell face is halfway between q_{ik_L} and q_{ik_R}. Consequently, as Nishikawa has shown [13], when the cell-face centroid is **not** halfway between and on the line drawn between the left, k_L, and right, k_R, cell centroids, the χ = 1/3 scheme can be substantially less accurate than the 2nd-order accurate χ = 0 scheme. This makes the use of U-MUSCL problematic for cell-centered schemes where the cell face is not guaranteed to be halfway between the left and right cell centroids as well as on the line drawn between the cell centroid, as illustrated in Fig. 2-b. However, Nishikawa proposed a linearity preserving version of U-MUSCL, i.e., LP-U-MUSCL [13], that recovers 2nd-order accuracy on irregular grids. Figure 3 shows that for an interface between two triangles where the interface is not halfway between the cell centroids, the state variables can be constructed at alternative locations labeled as k_L' and k_R' using Fromm's scheme, that are constructed such that the cell interface lies halfway between k_L and k_R' when reconstructing the left state, and halfway between k_L' and k_R when reconstructing the right state. This intermediate reconstruction step can be combined with Eqs. (3,4) to yield the LP-U-MUSCL scheme where the left state is computed using

$$q_{if}^{L} = \frac{\kappa}{2}(q_{k_L} + q_{k'_R}) + (1-\kappa)[q_{k_L} + \overline{\nabla q}_i^{L} \cdot \vec{r}_{Lf}] \quad (5)$$

and

$$q_{k'_R} = q_{k_R} + \overline{\nabla q}_i^{R} \cdot [r_{f_c} + (r_{f_c} - r_{k_L}) - r_{k_R}]. \quad (6)$$

Similarly, the right state is computed using

$$q_{if}^{R} = \frac{\kappa}{2}(q_{k_R} - q_{k'_L}) + (1-\kappa)[q_{k_R} + \overline{\nabla q}_i^{R} \cdot \vec{r}_{Rf}] \quad (7)$$

and

$$q_{k'_L} = q_{k_L} + \overline{\nabla q}_i^{L} \cdot [r_{f_c} + (r_{f_c} - r_{k_R}) - r_{k_L}]. \quad (8)$$

Note that χ has been replaced by κ to indicate LP-U-MUSCL. The 1-D accuracy for κ are defined as

κ = 0, gives Fromm's scheme, gives a 2nd-order scheme,
κ = -1, gives a 2nd-order fully upwind scheme,
κ = 1/3, gives a 3rd-order upwind biased scheme,

which, due to our use of one point flux quadrature, results in these schemes being 2nd-order accurate schemes in 2-D and 3-D.

C. Role of the Gradient in Viscous Flux Construction.

The computation of the viscous flux requires that the cell-face average viscous primitive variable, $\overline{q_{v,f}}$, and the cell-face average gradient of the viscous primitive variables, $\overline{\nabla q}_{v,f}$, be computed, where the viscous primitive variables are,

$$q_{vf} = (\frac{\rho_1}{\rho}, \ldots, \frac{\rho_{ncs}}{\rho}, \rho, u, v, w, T, k, \omega) \quad \text{for thermal equilibrium, or,}$$

$$q_{vf} = (\frac{\rho_1}{\rho}, \ldots, \frac{\rho_{ncs}}{\rho}, \rho, u, v, w, T_{ve}, T_{tr}, k, \omega) \quad \text{for thermal nonequilibrium,}$$

with T, T_{ve} and T_{tr} being the static, vibrational/electronic and translational/rotational temperatures, respectively. We have found that the construction of $\overline{q_{vf}}$, should be consistent with the method used to compute the cell-face gradient of the primitive variable, therefore, we begin by describing the methods that can be used to construct the cell-face gradient. Hasselbacher [27] observed that computing $\overline{\nabla q}_{vf}$ as a simple average of the left and right face gradients, i.e.,

$$\overline{\nabla q}_{vf} = \frac{(\overline{\nabla q}_v^{L} + \overline{\nabla q}_v^{R})}{2}, \quad (9)$$

leads to odd-even decoupling, which can be alleviated through the introduction of face-derivative augmentation. Hasselbacher suggested two methods to accomplish this augmentation; 1) edge-normal (*EN*) and 2) face-tangent (*FT*) cell-face gradient augmentation methods. The edge-normal and face-tangent augmented cell-face gradient methods

were studied in Refs. [4,15,28], where the face-tangent method was found to be preferable to the edge-normal method. Moreover, in Ref. [15], the observation was made that, in many cases, a converged solution could only be obtained when the face-tangent augmented face-gradient method was used. Therefore, since the edge-normal augmented cell-face gradient method does not result in a robust method on skewed grids it will not be considered further. In a cell-centered context, we define the cell-face viscous primitive variable and face-tangent augmented cell-face gradient, $\overline{q_{vf}}$, and $\widehat{\nabla q}_{vf}^{FT}$, respectively as

$$\overline{q_{vf}} = \frac{(q_{vk_L}+q_{vk_R})}{2} \text{ and } \widehat{\nabla q}_{vf}^{FT} = \overline{\nabla q}_{vf} - [(\overline{\nabla q}_{vf} \cdot \hat{e}_{LR}) - \frac{(q_{vk_R} - q_{vk_L})}{|\vec{e}_{LR}|}](\frac{\hat{n}_f}{\hat{n}_f \cdot \hat{e}_{LR}}) \quad , \tag{10}$$

where q_{vk_L} and q_{vk_R} are the left and right cell viscous primitive variables, $\hat{n}_f$, is the cell-face unit normal vector, and the vector connecting the left and right cell centroids, $\vec{e}_{LR}$ and its unit vector $\hat{e}_{LR}$ are defined in Fig. 2-b. More recently, Nishikawa [29] proposed a new approach where the cell-face gradient construction approach is derived from an advection scheme applied to a hyperbolic diffusion model. The resulting viscous diffusion scheme has a consistent approximation term and an adjustable high-frequency damping term with a coefficient alpha, and thus, is referred herein as the alpha-damped scheme. Nishikawa has shown that the Haselbacher augmentation terms, the bracketed terms in Eq. (10), can be interpreted as a high-frequency error damping term. Furthermore, Nishikawa makes the observation that this damping term is why the face-tangent method is a robust scheme on highly skewed meshes. Nishikawa attributes this robustness to the face-tangent schemes dependence on the cell skewness term, $1/(\hat{n}_f \cdot \hat{e}_{LR})$, which as skewness increases, $(\hat{n}_f \cdot \hat{e}_{LR})$ decreases, thereby increasing damping.

When Nishikawa's hyperbolic diffusion-based approach [29] is applied to a cell-centered, finite-volume scheme, it results in a reconstruction-based cell-face average gradient, $\widehat{\nabla q}_{vf}^{AD}$, that includes a damping term that arises naturally due to an upwind method being used to discretize a hyperbolic diffusion system followed by the extraction of a scalar diffusion scheme. In this reconstruction-based cell-face average gradient method, also known as, the alpha-damped scheme, $\overline{q_{vf}}$, and $\widehat{\nabla q}_{vf}^{AD}$, have the form

$$\overline{q_{vf}} = \frac{(q_{vf}^L+q_{vf}^R)}{2} \text{ and } \widehat{\nabla q}_{vf}^{AD} = \overline{\nabla q}_{vf} + \alpha(\frac{\hat{n}_f}{|\vec{e}_{LR} \cdot \hat{n}_f|})(q_{vf}^R - q_{vf}^L) \quad , \tag{11}$$

where α is a damping coefficient and q_{vf}^L and q_{vf}^R are the left and right higher-order-reconstructed viscous face state variables. These state variables are reconstructed using Fromm's scheme where

$$q_{vf}^L = q_{vk_L} + \overline{\nabla q}_v^L \cdot \vec{r}_{Lf}, \tag{12}$$

$$q_{vf}^R = q_{vk_R} + \overline{\nabla q}_v^R \cdot \vec{r}_{Rf}. \tag{13}$$

The $\overline{\nabla q}_{vf}$ term in Eq. (11), is the consistent term that approximates the face gradient, and the $\alpha(\frac{\hat{n}_f}{|\vec{e}_{LR} \cdot \hat{n}_f|})(q_{vf}^R - q_{vf}^L)$ term is the adjustable damping term. Note that the alpha-damping scheme reduces to the face-tangent method when 1) the reconstruction is performed halfway between the two centroids across the face, instead of at the face, 2) the absolute value is removed from the skewness measure in the denominator, and 3) $\alpha = 1$.

D. Construction of Gradients for Inviscid Flux, Viscous Flux and Source Terms.

Equations (1-9) reveal that the inviscid and viscous fluxes require that left and right gradients, $\overline{\nabla q}_i^L, \overline{\nabla q}_i^R$, and $\overline{\nabla q}_v^L, \overline{\nabla q}_v^R$ of the inviscid and viscous primitive variables be computed. Moreover, the computation of turbulent flow requires the computation of cell-average gradients of the viscous primitive variables for the construction of the turbulence model source terms. Therefore, a discussion regarding possible approaches using the linear WLSQ method to compute these gradients, follows.

D.1. Cell-centered weighted least-squares gradients using a cell-centered solution.

The state of the art for the direct computation of cell-centered gradients has been the subject of extensive research [4-7,15-19]. For a detailed description of the most popular cell-average gradient linear WLSQ methods as well as a recently developed method based on an analysis of the least-squares coefficient matrix the reader is directed to Refs. [4 -7]. In the current work, we will consider the most popular cell-average gradient stencils. These are the face neighbor of face neighbors (*fn2*-CCG) and node neighbor (*nn*-CCG) cell-centered gradient stencils illustrated in Figs. 4 and 5, respectively.

D.2. Node-centered weighted least-squares gradients using a cell-centered cell-average solution.

Zhang [20-22] proposed a linear WLSQ 2-D method where the gradients are computed at the nodes and averaged to the cells. Figure 6 presents the stencils required to define the gradients at the nodes, $j=1, 2, \ldots, N_{cell(k)}^{nodes}$ for a cell, *k*, where, $N_{cell(k)}^{nodes}$, is the number of nodes that surround cell *k*, on grids made up of triangular and quadrilateral control volumes, respectively. These nodal gradients can, in turn, be used to construct face-averaged nodal gradients (F-

ANG), and the cell-averaged nodal gradients (C-ANG) [7,10]. To compute the gradient of a solution variable q at a node, j, we use the set, $\{l_j\}$ of $N_j \geq 4$, of the nearby cells that share the node (i.e., a gradient stencil). It is important to note that the solution values are not available at the nodes because numerical solutions are stored at cells in the cell-centered finite-volume method. As pointed out by Zhang [20-22], the solution value at the node is included as an additional unknown when formulating the least-squares problem. Therefore, in 3-D, for node-centered linear WLSQ, we fit a linear polynomial over $\{l_j\}$ such that:

$$q_l = q_j + \overline{\partial_x q_j} dx_{l,j} + \overline{\partial_y q_j} dy_{l,j} + \overline{\partial_z q_j} dz_{l,j} \quad , \quad l \in \{l_j\}, \tag{14}$$

where, $dx_{l,j} = (x_l - x_j)$, $dy_{l,j} = (y_l - y_j)$, and $dz_{l,j} = (z_l - z_j)$, are the distance from node j to cell l of the set of neighbor cells, l, (x_j, y_j, z_j) and (x_l, y_l, z_l) denote the coordinates of the node, j, and cell, l, respectively, and $\left(q_j, \overline{\partial_x q_j}, \overline{\partial_y q_j}, \overline{\partial_z q_j}\right)$ is the vector containing the solution and its derivative that we wish to compute at node j. To determine the unknowns, we need at least three and four cells around the node in 2-D and 3-D, respectively. For interior nodes, such as shown in Fig. 6, there are always sufficient cells available for the LSQ problem to be solved. Following Zhang [20-22], we employ the linear WLSQ formulation:

$$\boldsymbol{A}x = b, \tag{15}$$

where

$$A = \begin{bmatrix} w_1^n & w_1^n dx_{1,j} & w_1^n dy_{1,j} & w_1^n dz_{1,j} \\ \vdots & \vdots & \vdots & \vdots \\ w_l^n & w_l^n dx_{l,j} & w_l^n dy_{l,j} & w_l^n dz_{l,j} \\ \vdots & \vdots & \vdots & \vdots \\ w_{N_j}^n & w_{N_j}^n dx_{N_j,j} & w_{N_j}^n dy_{N_j,j} & w_{N_j}^n dz_{N_j,j} \end{bmatrix}, \quad x = \begin{bmatrix} q_j \\ \overline{\partial_x q_j} \\ \overline{\partial_y q_j} \\ \overline{\partial_z q_j} \end{bmatrix}, \quad b = \begin{bmatrix} w_1^n q_1 \\ \vdots \\ w_l^n q_l \\ \vdots \\ w_{N_k}^n q_{N_j} \end{bmatrix}, \tag{16}$$

$l=1\text{-}N_j$ are the cells in the stencil of node j, and w_l^n is the weight applied to the equation corresponding to the stencil cell l. The following inverse-distance weight is widely used in finite-volume methods:

$$w_l^n = \frac{1}{d_l^{p(n)}} \quad , \quad d_l = \sqrt{dx_{l,j}^2 + dy_{l,j}^2 + dz_{l,j}^2} \quad , \tag{17}$$

where $p(n)$ is a parameter ranging from zero (unweighted LSQ) to one (fully weighted LSQ) and n =1, 2, or 3, where n=1 refers to the parameter used for the linear WLSQ gradients used in the inviscid flux reconstruction, n=2 refers to the parameter used for the linear WLSQ gradients used in the construction of the cell-face gradients for the viscous flux and n=3 refers to the parameter used for the linear WLSQ gradients used in the construction of turbulence model source terms. In our work, we typically set p(1)=0 and p(2,3)=1. The overdetermined linear WLSQ system defined by Eqs. (15-17), can be solved in various ways. However, we choose to use QR factorization via the Householder transformation [30], which directly solves the over determined system as

$$x = R^{-1} Q b, \tag{18}$$

where Q is the orthonormal matrix and R is the upper triangular matrix generated from $\boldsymbol{A}$ by the QR factorization. The solution can then be expressed in the following form:

$$\overline{\nabla q_j} = \begin{bmatrix} q_j \\ \overline{\partial_x q_j} \\ \overline{\partial_y q_j} \\ \overline{\partial_z q_j} \end{bmatrix} = \sum_{l \in \{l_j\}} \begin{bmatrix} c_{jl}^q \\ c_{jl}^x \\ c_{jl}^y \\ c_{jl}^z \end{bmatrix} q_l \quad , \tag{19}$$

where c^q_{jl}, c^x_{jl}, c^y_{jl}, and c^z_{jl} are the linear WLSQ coefficients to be computed and stored at all nodes once for a given stationary grid. From Eq. (19), it is clear that the cost of the gradient calculation is directly proportional to the number of neighbors involved in the node WLSQ stencil. Furthermore, since we choose to not use the solution value at the node, we only need to store the coefficients for the gradient, such that:

$$\overline{\nabla q_j} = \begin{bmatrix} \overline{\partial_x q_j} \\ \overline{\partial_y q_j} \\ \overline{\partial_z q_j} \end{bmatrix} = \sum_{l \in \{l_j\}} \begin{bmatrix} c_{jl}^x \\ c_{jl}^y \\ c_{jl}^z \end{bmatrix} q_l \quad . \tag{20}$$

As previously mentioned, there are 3 approaches that use nodal gradients to compute the gradients needed to compute the cell-face fluxes. These are the C-ANG approach of Zhang [20-22], which he refers to as a vertex-weighted least-squares (VWLSQ(n)) approach where n is the least-squares weight coefficient, the F-ANG approach of Nishikawa and White [9] and the F-ANG+fn augmented approach of Nishikawa and White[11].

In the C-ANG approach, the inviscid and viscous cell-nodal-averaged gradients, $\overline{\nabla q_{ik}}$ and $\overline{\nabla q_{vk}}$, respectively, are constructed as the arithmetic average of the nodal gradients from the nodes that define the cell with

$$\overline{\nabla q_{ik}} = \left[\sum_{j=1}^{N_{cell(k)}^{nodes}} \overline{\nabla q_{ij}} \right] / N_{cell(k)}^{nodes} \quad , \tag{21}$$

$$\overline{\nabla q}_{vk} = [\sum_{j=1}^{N_{cell(k)}^{nodes}} \overline{\nabla q}_{vj}\ ] / N_{cell(k)}^{nodes}\ , \tag{22}$$

where $N_{cell(k)}^{nodes}$ is 3 or 4 in 2-D for triangles or quadrilaterals cells, respectively, and 4, 5, 6 or 8 in 3-D for tetrahedral, pyramidal, prismatic or hexahedral cells, respectively. These cell average gradients are then used to define the inviscid and viscous left and right gradients, $\overline{\nabla q}_i^L, \overline{\nabla q}_v^L, \overline{\nabla q}_i^R$, and $\overline{\nabla q}_v^R$ that appear in Eqs. (1-13) to compute the inviscid and viscous fluxes where

$$\overline{\nabla q}_i^L = \overline{\nabla q}_{ik_L} \text{ and } \overline{\nabla q}_i^R = \overline{\nabla q}_{ik_R} \tag{23}$$

$$\overline{\nabla q}_v^L = \overline{\nabla q}_{vk_L} \text{ and } \overline{\nabla q}_v^R = \overline{\nabla q}_{vk_R} \tag{24}$$

where $\overline{\nabla q}_{ik_L}, \overline{\nabla q}_{ik_R}$ and $\overline{\nabla q}_{vk_L}, \overline{\nabla q}_{vk_R}$ are the left and right, inviscid and viscous, C-ANG WLSQ gradients respectively, defined by Eqs. (20,21,22).

In the F-ANG approach, the inviscid and viscous face nodal averaged-gradients, $\overline{\nabla q}_{if}$ and $\overline{\nabla q}_{vf}$, respectively, are computed as the arithmetic average of the nodal gradients from the nodes that define the cell face with

$$\overline{\nabla q}_{if} = [\sum_{j=1}^{N_{face(m)}^{nodes}} \overline{\nabla q}_{ij}\ ] / N_{face(m)}^{nodes}\ , \tag{25}$$

$$\overline{\nabla q}_{vf} = [\sum_{j=1}^{N_{face(m)}^{nodes}} \overline{\nabla q}_{vj}\ ] / N_{face(m)}^{nodes}\ , \tag{26}$$

where $N_{face(m)}^{nodes}$ is the number of nodes that define a face, m, which is 2 in 2-D, and 3 or 4 in 3-D for triangular and quadrilateral faces, respectively. These face-averaged gradients, are then used to define the left and right inviscid and viscous gradients, $\overline{\nabla q}_i^L, \overline{\nabla q}_i^R$ and $\overline{\nabla q}_v^L, \overline{\nabla q}_v^R$ that appear in Eqs. (1-13). As was noted in Refs. [8-10], the F-ANG approach results in the following condition with respect to the left and right inviscid and viscous gradients

$$\overline{\nabla q}_i^L = \overline{\nabla q}_i^R = \overline{\nabla q}_{if}\ , \tag{27}$$

$$\overline{\nabla q}_v^L = \overline{\nabla q}_v^R = \overline{\nabla q}_{vf}\ . \tag{28}$$

There are three reasons that the average nodal gradient approach is potentially superior to the conventional cell-average gradient method. First, the number of nodes is typically smaller than the number of cells in unstructured grids, especially in 3-D on tetrahedral grids, where it is 5-6 times smaller, thus requiring less storage for the gradients (if one chooses to store them). Moreover, if the nodal gradients are computed using a least-squares method, as described in Eqs. (14-20), using the cells surrounding the node, the number of coefficients that need to be computed and stored can be significantly smaller than that required for the cell-centered least-squares method for cell gradients described in section *D.1*. Second, the face gradient involves fewer cells than the average of cell gradients at a face, which results in a reduction in the size of the residual stencil and third, since the gradients are computed at the cell nodes, then, depending on how the gradient limiting is performed, there may be no need to communicate gradient information between processors.

*D.2.1. Stable Techniques for Using **Unaugmented** Node-Centered Gradients to Construct the Inviscid Flux.*

In the case of the 2-D hybrid grid cell face shown in red in Fig. 1, three approaches for computing the gradients required to construct the inviscid flux at the cell face are illustrated in Fig. 7, where *lt* and *lq* denote stencil cells associated with triangular and quadrilateral cells, respectively. The three approaches are: a) the F-ANG approach [10], b) the C-ANG approach [20-22], and c) the hybrid face and cell-averaged nodal gradient approach (FAC-ANG) in Ref. [8,9]. Figure 7-a shows that F-ANG results in the most compact flux stencil while Fig. 7-b shows that C-ANG results in the least compact stencil. In Ref. [9], it was shown, via Fourier analysis, that inviscid fluxes computed using F-ANG are unstable on quadrilateral grids, implying that computing inviscid fluxes using F-ANG will also be unstable on hybrid grids containing quadrilaterals. However, Zhang has shown in Refs. [20,21] that the C-ANG approach is stable on triangular, quadrilateral, and hybrid grids. Therefore, to obtain a stable inviscid flux and the smallest possible residual stencil on hybrid grids, the FAC-ANG approach was proposed in Ref. [9]. FAC-ANG, as illustrated in Fig. 7-c, uses F-ANG for the on the triangular cell side of the red interface and C-ANG for the on the quadrilateral cell side of the red interface. The extension of FAC-ANG to 3-D on hybrid grids that may include tetrahedral, pyramidal, prismatic and/or hexahedral cells is more complicated and can be found in Ref. [8].

*D.2.2. Stable Techniques for Using **Augmented** Node-Centered Gradients to Construct the Inviscid Flux.*

Recently a new approach to using node-centered gradients on hybrid grids in 2-D that allows the F-ANG approach to be used on triangles and quadrilaterals was described in Ref. [11]. This approach is based on augmenting the baseline node-centered stencil with face-neighbor cells of the cells that define the node-centered gradient stencil. Figures 8-a and 9-a show several possible stencils around a node in triangular- and quadrilateral-based grids. The cells tagged with a black number 2 are the baseline F-ANG stencil cells and cells tagged with a green number 3 are the

aforementioned face neighbor (*fn*) cells. There are also cells tagged with a red number 4 that are the cells that are node-neighbors (*nn*) of the cells that define the node-centered gradient stencil that are not already tagged as cell face-neighbors. We choose to adopt a stencil naming convention where F-ANG+*fn* refers to the stencil that is the sum of the cells tagged 2 and 3 and FANG+*nn* refers to the stencil that is the sum of the cells tagged as 2, 3 and 4. Likewise, Figures 8-b and 9-b present the residual stencil of the F-ANG+*fn* and FANG+*nn* stencils. The stability of F-ANG+*fn* for advection on regular quadrilaterals was demonstrated by Nishikawa and White in Ref. [11] using Fourier analysis. Moreover, numerical experiments performed in Ref. [11] demonstrated that F-ANG+*fn* outperformed all previously tested approaches on 2-D high aspect ratio highly curved grids. Figures 10-a and b present a comparison of the FAC-ANG and C-ANG face node stencils with the F-ANG+*fn* and F-ANG+*nn* face node stencils applied to a 2-D hybrid grid. This comparison shows that the F-ANG+ face stencils are bigger than the FAC-ANG stencil and C-ANG stencils. Experience has shown, in 2-D and 3-D, that bigger stencils are usually more stable than smaller stencils. Therefore, since the FAC-ANG and C-ANG approaches have been demonstrated to be stable for advection in 2-D and 3-D, and the F-ANG+*fn* approach has been demonstrated to be stable via analysis and numerical experiments in 2-D, it seems reasonable that this approach will also be stable for advection in 3-D on hybrid grids due to its bigger stencil.

*D.2.3. Stable Techniques for Using **Augmented** Node-Centered Stencils to improve the accuracy of the gradients.*

Recognizing that that the augmented F-ANG stencils are bigger and therefore more expensive, we attempt to take advantage of the bigger stencil to increase accuracy by using quadratic WLSQ instead of linear WLSQ when the stencil is big enough. To compute the WLSQ gradient of a solution variable q at a node, j, we use the set, $\{l_j\}$ of $N_j \geq 10$, cells near the node. Using the same notation as in Eqs. (14-17) a 3-D node centered quadratic WLSQ fit may be derived by fitting a quadratic polynomial over the set of cells near the node j, $\{l_j\}$ such that:

$$q_l = q_j + \overline{\partial_x q}_j dx_{l,j} + \overline{\partial_y q}_j dy_{l,j} + \overline{\partial_z q}_j dz_{l,j} + \frac{1}{2}\overline{\partial_x^2 q}_j dx_{l,j}^2 + \frac{1}{2}\overline{\partial_y^2 q}_j dy_{l,j}^2 + \frac{1}{2}\overline{\partial_z^2 q}_j dz_{l,j}^2 + \overline{\partial_{xy} q}_j dxdy_{l,j} + \overline{\partial_{xz} q}_j dxdz_{l,j} + \overline{\partial_{yz} q}_j dydz_{l,j} \quad ,$$

$$l \in \{l_j\}, \tag{29}$$

where, $dxdy_{l,j} = (x_l - x_j)(y_l - y_j)$, $dxdz_{l,j} = (x_l - x_j)(z_l - z_j)$, and $dydz_{l,j} = (y_l - y_j)(z_l - z_j)$, are the cross products of the Cartesian distances from the node j to the cells, l. and $\left(q_j, \overline{\partial_x q}_j, \overline{\partial_y q}_j, \overline{\partial_z q}_j, \overline{\partial_x^2 q}_j, \overline{\partial_y^2 q}_j, \overline{\partial_z^2 q}_j, \overline{\partial_{xy} q}_j, \overline{\partial_{xz} q}_j, \overline{\partial_{yz} q}_j\right)$ is the vector containing the solution and its first and second derivatives. As in the linear WLSQ formulation, we employ the quadratic WLSQ formulation written as

$$\boldsymbol{A}x = b, \tag{30}$$

where

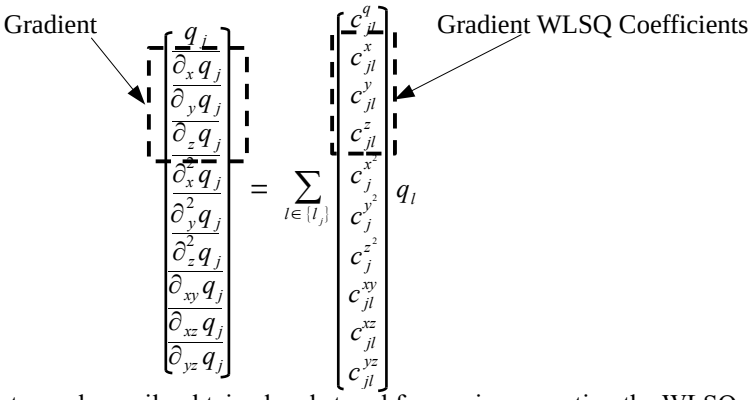
$$A = \begin{bmatrix} w_1^n & w_1^n dx_{1,j} & w_1^n dy_{1,j} & w_1^n dz_{1,j} & \frac{1}{2} w_1^n dx_{1,j}^2 & \frac{1}{2} w_1^n dy_{1,j}^2 & \frac{1}{2} w_1^n dz_{1,j}^2 & w_1^n dxdy_{1,j} & w_1^n dxdz_{1,j} & w_1^n dydz_{1,j} \\ \vdots & \vdots & \vdots & \vdots & \vdots & \vdots & \vdots & \vdots & \vdots & \vdots \\ w_l^n & w_l^n dx_{l,j} & w_l^n dy_{l,j} & w_l^n dz_{l,j} & \frac{1}{2} w_l^n dx_{l,j}^2 & \frac{1}{2} w_l^n dy_{l,j}^2 & \frac{1}{2} w_l^n dz_{l,j}^2 & w_l^n dxdy_{l,j} & w_l^n dxdz_{l,j} & w_l^n dydz_{l,j} \\ \vdots & \vdots & \vdots & \vdots & \vdots & \vdots & \vdots & \vdots & \vdots & \vdots \\ w_{N_j}^n & w_{N_j}^n dx_{N_j,j} & w_{N_j}^n dy_{N_j,j} & w_{N_j}^n dz_{N_j,j} & \frac{1}{2} w_{N_j}^n dx_{N_j,j}^2 & \frac{1}{2} w_{N_j}^n dy_{N_j,j}^2 & \frac{1}{2} w_{N_j}^n dz_{N_j,j}^2 & w_{N_j}^n dxdy_{N_j,j} & w_{N_j}^n dxdz_{N_j,j} & w_{N_j}^n dydz_{N_j,j} \end{bmatrix},$$

$$x = \begin{bmatrix} q_j \\ \overline{\partial_x q}_j \\ \overline{\partial_y q}_j \\ \overline{\partial_z q}_j \\ \overline{\partial_x^2 q}_j \\ \overline{\partial_y^2 q}_j \\ \overline{\partial_z^2 q}_j \\ \overline{\partial_{xy}^2 q}_j \\ \overline{\partial_{xz}^2 q}_j \\ \overline{\partial_{yz}^2 q}_j \end{bmatrix}, \quad b = \begin{bmatrix} w_1^n q_1 \\ \vdots \\ w_l^n q_l \\ \vdots \\ w_{N_j}^n q_{N_j} \end{bmatrix}, \tag{31}$$

As with linear WLSQ we solve this set of equations using QR factorization. However, since we

1. Do not require the solution at the nodes and
2. are using a 2nd-order method and thus only require the gradient.

we only need to store the least squares coefficients required to compute the gradient. From Eq.(20), these coefficients are c_{jl}^x, c_{jl}^y and c_{jl}^z. Comparing these coefficients to the coefficients that can be obtained by solving the quadratic WLSQ problem. Equation (32) reveals that the gradient coefficients we require are the 2nd, 3rd, and 4th entries in the column vector.



$$\begin{bmatrix} q_j \\ \partial_x q_j \\ \partial_y q_j \\ \partial_z q_j \\ \partial_x^2 q_j \\ \partial_y^2 q_j \\ \partial_z^2 q_j \\ \partial_{xy} q_j \\ \partial_{xz} q_j \\ \partial_{yz} q_j \end{bmatrix} = \sum_{l \in \{l_j\}} \begin{bmatrix} c_{jl}^{q} \\ c_{jl}^{x} \\ c_{jl}^{y} \\ c_{jl}^{z} \\ c_{j}^{x^2} \\ c_{j}^{y^2} \\ c_{j}^{z^2} \\ c_{jl}^{xy} \\ c_{jl}^{xz} \\ c_{jl}^{yz} \end{bmatrix} q_l \tag{32}$$

Therefore the gradient coefficients can be easily obtained and stored for use in computing the WLSQ gradient from the coefficients that result from the solution of the quadratic WLSQ problem. This means that

1. The storage needed to compute the gradient does not change whether one is using linear or the quadratic WLSQ.
2. The code needed to compute the gradient is the same whether one is using linear or the quadratic WLSQ.
3. The cost associated with using quadratic WLSQ to compute the gradient is only a one time preprocessing cost associated with solving the quadratic WLSQ problem to obtain the coefficients required to compute the gradient.

The absolute minimum number of cells required to compute the node centered quadratic WLSQ is 10. However, experience has shown that it is preferable to compute the gradient using the quadratic WLSQ coefficients when the stencil contains 25 cells or greater. Therefore, when computing the WLSQ coefficients, the linear WLSQ problem is solved if the node-centered stencil contains less than 25 cells and the quadratic WLSQ problem is solved if the stencil contains at least 25 cells. Table 1 presents the max stencil sizes for a regular tetrahedral grid constructed from a hexahedral grid where there are 6 tetrahedra per hexahedral cell and a hexahedral grid for the F-ANG, F-ANG+*nf* and F-ANG+*nn* stencils.

Table 1 Stencil statistics for hexahedral and regular tetrahedral grids.

	F-ANG	**F-ANG+*nf***	**F-ANG+*nn***
Hexahedral cells	8	32	64
Regular Tetrahedral cells	24	48	192

This table clearly demonstrates that either of the augmented node-centered gradient stencils are large enough to effectively support the computation of gradients using the WLSQ coefficients obtained by solving a quadratic WLSQ problem. Moreover on tetrahedral grid the F-ANG+*nn* stencil should only be used when it is not possible to get a well posed stencil with either F-ANG or F-ANG+*nf* due to its extremely large size.

D.2.4 Stable Techniques for Using Node-Centered Gradients to Construct the Viscous Flux.

In Ref. [9], it was shown that using F-ANG to compute the viscous fluxes is stable for any cell topology due to the damping terms in the viscous flux construction Eqs. (10,11). This is the approach adopted for computing 3-D flow in this work.

D.2.5. Construction of Gradients for Turbulence Transport Equation Source Terms.

The turbulence transport equation source terms require the computation of cell-average gradients of the viscous variables. In the current work, these gradients are formed using the cell average of the viscous WLSQ node-centered gradients. These node-centered gradients are only needed for the cells in the interior of the computational domain eliminating the need to communicate them between processors when using a parallel processing paradigm.

E. Inviscid Flux Cell-Average Gradient Limiter Construction using LP-U-MUSCL.

Being primarily interested in the computation of hypersonic flows containing strong discontinuities, gradient limiters are crucial to the development of a robust numerical scheme. Therefore, the current gradient limiter approach is based on the modified version of *MLP* approach of Park and Kim [12] extensively described in Refs. [4,6,7,8]. The *MLP* gradient limiter stencil for reconstruction at a cell face on a mixed-element grid, when using node-centered gradients, is illustrated in Fig. 8-11 where the limited left- and right-reconstructed states can be obtained using Fromm's scheme

$$q_{if}^{L} = q_{ik_L} + \Phi_{k_L}^{MLP} \overline{\nabla q_i}^{L} \cdot \vec{r}_{Lf} \tag{33}$$

$$q_{if}^{R} = q_{ik_R} + \Phi_{k_R}^{MLP} \overline{\nabla q_i}^{R} \cdot \vec{r}_{Rf} \tag{34}$$

where $\Phi_{k_L}^{MLP}$ and $\Phi_{k_R}^{MLP}$ are limiter functions at cells kL and kR, respectively. Due to our interest in the LP-U-MUSCL scheme, we employ a suggestion from Ref.[13], where Eqs.(5,7) are rewritten to incorporate a gradient limiter such that

$$\overline{q_{if}^{L}} = q_{k_L} + \Phi_{k_L}^{MLP}\{\Phi_{k_L}^{MLP}\frac{\kappa}{2}(q_{k_L} - q_{k'_R}) + (1-\kappa)[\overline{\nabla q_i}^{L} \cdot (r_{f_c} - r_{k_L})]\} \quad , \tag{35}$$

$$q_{k'_R} = q_{k_R} + \overline{\nabla q_i}^{R} \cdot [r_{f_c} + (r_{f_c} - r_{k_L}) - r_{k_R}] \qquad \text{and} \tag{36}$$

$$\overline{q_{if}^{R}} = q_{k_L} + \Phi_{k_R}^{MLP}\{\Phi_{k_R}^{MLP}\frac{\kappa}{2}(q_{k_R} - q_{k'_L}) + (1-\kappa)[\overline{\nabla q_i}^{R} \cdot (r_{f_c} - r_{k_R})]\} \quad , \tag{37}$$

$$q_{k'_L} = q_{k_L} + \overline{\nabla q_i}^{L} \cdot [r_{f_c} + (r_{f_c} - r_{k_R}) - r_{k_L}] \tag{38}$$

where $\Phi_{k_L}^{MLP}$ and $\Phi_{k_R}^{MLP}$ are *MLP* gradient limiter coefficients evaluated for the left and right cells when any gradient construction approach is used to form $\overline{\nabla q_i}^{L}$ or $\overline{\nabla q_i}^{R}$. The "original" MLP limiter coefficient approach, described in detail in Ref. [7], constructs the limiter coefficient by looping over cells and then looping over the nodes that define the cell using Fromm's scheme to reconstruct the primitive variables to the nodes as shown in Fig. 11-a. However, when using the LP-U-MUSCL scheme to reconstruct the primitive variables for the inviscid flux, using Fromm's scheme to perform the reconstruction in the limiter is inconsistent. Therefore, in an effort to make the limiter reconstruction consistent with the inviscid flux reconstruction, we revisit an idea originally presented in Ref. [9] where the limiter is constructed by looping over the nodes that define the face inside of a loop over faces, as shown in Fig. 11-b. In this loop over faces approach, the limiter coefficients in the left and right cell, $\Phi_{k_{LR}}^{MLP}$ at the cell and the left and right limiter coefficients each node that define the face, $\Psi_{n,m}^{L,R}$, are computed for each pair of cells that share a face, ie. the left (L) and right (R) cells using

$$\Phi_{k_{L,R}}^{MLP} = min\left(1, min\left(1, [\Psi_{n,m}^{L,R}, n=1 \rightarrow N_{nodes}^{m}]\right), m=1, \rightarrow N_{faces}\right), \tag{39}$$

$$\Psi_{n,m}^{L,R} = \begin{cases} \phi_{L,R}\left(\dfrac{q_m^{max(face\ node\ stencil\ cells)} - q_{k_{L,R}^m}}{q_{if_m}^{L,R} - q_{k_{L,R}^m}}\right), & \text{if } q_{if_m}^{L,R} > q_{k_{L,R}^m} \\ \phi_{L,R}\left(\dfrac{q_m^{min(face\ node\ stencil\ cells)} - q_{k_{L,R}^m}}{q_{if_m}^{L,R} - q_{k_{L,R}^m}}\right), & \text{else if } q_{if_m}^{L,R} < q_{k_{L,R}^m} \\ 1 & \text{else if } q_{if_m}^{L,R} = q_{k_{L,R}^m} \end{cases} . \tag{40}$$

where $q_{if_m}^{L,R}$ and $q_{k_{L,R}^m}$ are the left and right reconstruction of the solution to the cell node and the solution in the left and right cells respectively. It should be noted that the q_m^{min} and q^{max} in Eq. (40) are the minimum and maximum values of the solution in the cells that make up the union of the WLSQ gradient stencils at the nodes that define the cell face. The left and right cell limiter coefficients, Φ_{k_L,k_R}^{MLP}, are then computed as the minimum of the current cell coefficients and the left and right face node limiter coefficients. This looping over faces allows the use of LP-U-MUSCL in the limiter because, as is the case when reconstructing for the flux, the data from the both cells that share the face are available for use in Eqs. (39-40) to construct the limiter coefficients without an ambiguity. Finally, it is important to note that one drawback of this approach is that the node limiter coefficients are computed multiple times due to the nodes being shared between faces.

F. Additional Pressure Limiting.

In hypersonic flow, it has been noted by others [31-33] that due to the extremely strong shocks that can be encountered, it is sometimes necessary to add additional limiting at the shocks by incorporating a pressure based shock limiter. This limiter is sometimes referred to a pressure limiter. In our case, we incorporate a pressure limiter into our gradient limiter procedures. In the case of the LP-U-MUSCL face loop limiting procedure, we incorporate the approach described by Gnoffo[33] where the face pressure limiter is computed for the left and right cells using

$$\Psi_{p}^{L,R}=\begin{cases} 1 & if\ (\overline{\nabla P^{m}}\ \cdot\ \vec{V}\le 0) \\ 1/2\langle 1-\cos[\psi_{p}^{L,R}(P_{ratio})\pi]\rangle & if\ (\overline{\nabla P^{m}}\ \cdot\ \vec{V}>0) \end{cases} \tag{41}$$

where

$$\psi_{p}^{L,R}(P_{ratio})=\begin{cases} 1 & if\ (P_{ratio}\le 2) \\ (4-P_{ratio})/2 & if\ (2<P_{ratio}<4), \\ 0 & if\ (P_{ratio}\ge 4) \end{cases} \tag{42}$$

$$P_{ratio}=max(P_{f_m}^{L,R}/P_{m}^{max})/min(P_{f_m}^{L,R}/P_{m}^{min}), \tag{43}$$

and Eq. (39) is modified to be

$$\Phi_{k_{L,R}}^{MLP}=min(1,min(\Psi_{p}^{L,R},min([\Psi_{n,m}^{L,R},n=1\rightarrow N_{nodes}^{m}]),m=1,\rightarrow N_{faces})). \tag{44}$$

III Numerical Results and Discussion

A. 2-D Structured Grid Resolution Study of Hypersonic Laminar Flow Over a 2-D Flat Plate on a regular tetrahedral grid.

The first numerical experiment chosen to investigate the numerical behavior of the 3-D extension and implementation of F-ANG+ is performed on a family of regular tetrahedral grid for a canonical 2-D hypersonic laminar boundary layer flow. However, before computing these unstructured solutions, a "reference" solution is needed to allow the accuracy of the unstructured solutions to be assessed. Therefore, a 2-D grid resolution study was performed using the VULCAN-CFD 2-D structured grid solver on a family of 5, 2-D structured grids, consisting of 101x77, 201x153, 401x305, 801x609 and 1601x1217 grid nodes, respectively. Figure 12 presents a plot of the 101x77 grid used where every other grid line has been removed for clarity. This numerical experiment was conducted by computing thermally-prefect, chemically-frozen, turbulent flow of air over a 2-D flat plate with freestream conditions of Mach number, M_{ref}=6.0, static pressure, P_{ref}= 2100.0 Pa, static temperature, T_{ref}= 63.01 K, and unit Reynolds number, Re_{ref}= 2.64x107/m, with the wall treated as an isothermal (335.83 K) condition. These computations were performed using inviscid fluxes computed using Edward's LDFSS scheme [24] with reconstruction performed using a structured grid MUSCL scheme [39] with $\kappa=1/3$. No gradient limiters were used. The wall heat transfer distribution results using these 5 grids are presented in Fig. 13. Examination of Fig. 13 reveals that, although a grid resolved wall heat transfer distribution appears to have been achieved over the majority of the flat plate axial length using the 801x609 grid, we will use the 1601x1207 grid solution as our reference.

B. Hypersonic Laminar Flow Over a 2-D Flat Plate Using a Regular Tetrahedral Grid.

Having produced a reference 2-D solution, we now turn to the tetrahedral unstructured grid version of this problem. Since we are primarily interested in 3-D, we choose to use only tetrahedral grids since they are inherently 3-D even for 2-D geometries. The first 3-D numerical experiment was chosen to investigate the numerical behavior of the 3-D extension and implementation of F-ANG+ on a pure tetrahedral grid using a canonical 2-D hypersonic laminar boundary layer flow. This numerical experiment was conducted by computing thermally-prefect, chemically-frozen, turbulent flow of air over a 2-D flat plate with the same freestream conditions that were run to compute the "reference" solution. The inviscid fluxes were computed using Edward's LDFSS scheme [24] and LP-U-MUSCL [12] with $\kappa=0$ or $\kappa=1/3$. No gradient limiters were used. The viscous fluxes were computed using Nishikawa's alpha-damped scheme [28] with $\alpha=4/3$. The 2-D geometry was discretized to form a 3-D computational domain by generating a regular tetrahedral grid starting from a 3-D structured grid. A series of 3-D tetrahedral grids were generated from 51x39x3, 101x077x5, 201x153x9, and 401x305x17 node 3-D structured grids, which are, in turn, based on the 2-D structured girds used to compute the "reference" solution. The resulting tetrahedral grids contained 22,800, 182,400, 1,459,200 and 11,673,600 cells, respectively. An oblique view of the 51x39x3 node grid is shown in Fig. 14. The boundary conditions were: 1) reflection of all variables at the min. and max. Y-direction boundary cell faces, 2) specification of all variables on the min. X-direction boundary cell faces, 3) 1st-order extrapolation of all variables at the max. X- and Z-direction boundary cell faces and 4) a no-slip, isothermal, solve-to-the-wall BC on the min. Z-direction wall boundary cell faces. The computational domain was decomposed into 6 partitions for the smallest grid and 24 partitions for the remaining grids. The governing equations were solved implicitly, using local time stepping, and the global CFL number was linearly varied from 0.1 to 250 over iterations 1 to 500. A grid resolution study using the 4 unstructured grid described above was performed using the F-ANG+*fn* approach. Additional isolated computations were performed using the *nn*-CCG, F-ANG and F-ANG+*fn* approaches on the 201x153x9 node grid to allow the comparison of the various approaches under consideration.

Table 1 presents the stencil statistics of the *nn*-CCG and two node-centered F-ANG approaches for computations performed using this 201x153x9 node grid. In addition, the cost, and relative cost, of computing the WLSQ gradients, where the cost is defined as the number of WLSQ locations (the number of cells for the cell-centered gradient and the number of nodes for the node-centered gradient approaches, respectively), times the mean stencil size. These figures of merit show that the node-centered gradient approach produced stencils that are smaller than the *nn*-CCG approach in the mean. Table 1 also reveals that the F-ANG and F-ANG+*fn* approaches requires approximately 6.2% and 11.9% of the *nn*-CCG methods storage and operations to compute the gradients, respectively.

Table 1. Stencil statistics and cost of the gradient approaches used to compute the 2-D flat plate using a 201x153x9 node tetrahedral grid.

WLSQ Gradient Approach	Number of WLSQ Stencils	Minimum Stencil Size	Mean Stencil Size	Maximum Stencil Size	Stencil Size Standard Deviation	WLSQ Cost (No. of Stencils x Mean Stencil Size)	WLSQ Relative Cost
nn-CCG	1,459,200 (cells)	19	66.9	106	8.5	97,620,480	1.0
F-ANG	276,777 (nodes)	6	22.0	46	4.0	6,089,094	0.062
F-ANG+*fn*	276,777 (nodes)	8	42.0	91	10.0	11,624,634	0.119

Wall axial heat transfer results from the tetrahedral grid resolution study using the F-ANG+*fn* scheme are shown in Fig. 15-a. These results show that the wall axial heat transfer distribution is not grid converged between the leading edge and x=0.15 meters even on the finest grid. However for x=0.15 to the trailing edge the results look fairly well converged with the unstructured solver giving a wall heat transfer slightly higher than the structured solver. As mentioned above we then selected this 201x153x9 node tetrahedral grid and compare results using the *nn*-CCG, F-ANG and F-ANG+*fn* schemes. As shown in Figs. 15-b and 15-c, we find that all methods tested have similar accuracy. Only by magnifying the region near the trailing edge of the flat plate, as in Fig. 15-c, do we see differences in the solutions, with the F-ANG+*fn* giving solutions closest to the structured grid. Three of these solutions, using the *nn*-CCG, F-ANG and F-ANG+*fn* approaches were computed using $\kappa = 0$, and a fourth solution using the F-ANG+fn approach was computed using $\kappa = 1/3$. Figure 15-c reveals that the change in κ only slightly improved the solution, which is not surprising given that this is a diffusion dominated flow.

C. Hypersonic Laminar Flow Over a 2-D Flat Plate Using Output adapted Tetrahedral Grid.

As mentioned in the introduction the sketch-to-solution (*S2S*) grid adaptation workflow [1] using the ***refine*** grid adaptation code [2] has been developed. The infrastructure to support this approach was recently implemented in the VULCAN-CFD software suite [3] where an extensive discussion of the challenges and pitfalls of *S2S* are discussed. In the S2S approach, a final grid is arrived at by repeatedly adapting the grid to the solution using feature-based or adjoint-based adaptation repeatedly until some stopping criteria based on convergence of engineering figure(s) of merit is reached. As VULCAN-CFD does not currently support an adjoint capability, we have pursued the feature based approaches described in Ref. [3]. Since the current grid paradigm used within ***refine*** is tetrahedral-based we have been motivated to invest considerable effort [5-11] to develop cell-centered advection, diffusion and source term operators that are robust on highly skewed tetrahedral grids. The flat plate problem described in sections III-A and III-B above was therefore chosen to explore the ability of *S2S* to predict wall heat transfer with sufficient fidelity to serve as an engineering figure of merit. The numerical techniques utilized were the same as employed in the computations in section III-B above. In addition, the SGS defect-correction scheme was used instead of the more expensive JFNK procedure described in Ref. [3]. Because this test has a very weak leading edge shock, the grids were adapted to a total enthalpy Hessian. Figure 16 presents the wall heat transfer distribution obtained after 29 grid adaptations and a grid containing on the order of 6.4×10^5 tetrahedral cells while Fig. 17 presents several views of the tetrahedral unstructured adapted grid produced by ***refine***.

D. Hypersonic Turbulent Flow Over a 2-D Backward Facing Step Using Prismatic and Hexahedral Cells.

In order to test that all the F-ANG+ methods work properly on a mixed element grid and to demonstrate the behavior of the pressure limiter modification described in Eqs. 35-40, numerical experiments were conducted computing hypersonic calorically perfect, turbulent flow of air over a 2-D backward-facing step. The freestream conditions were, Mach 6.356, static pressure, P_{ref}= 50,662.58 Pa, static temperature, T_{ref}= 1297.75 K, ratio of specific heats, γ_{ref} = 1.4, and unit Reynolds number, Re_{ref}= 1.2891×10^7/m, with the wall treated as isothermal (1172.6 K), using a turbulent wall matching boundary condition [38]. The Wilcox (1998) $k-\omega$ two-equation turbulence model [38] was used to compute the Reynolds stresses and Reynolds heat flux (Pr_t=0.9) and the turbulence model production term was based on the magnitude of the vorticity. The nodal gradients were computed using weighted linear least-squares with the FANG+*fn* method. The inviscid fluxes were computed using the LDFSS scheme with the higher-order cell-face states constructed using LP-U-MUSCL, $\kappa = 1/3$, with the cell-average gradients limited using the loop over faces based approach to computing the κ consistent *MLP* gradient limiter approach illustrated in Fig. 11-b) and the Park and Kim *MLP-u2*

limiter function. The viscous fluxes were computed using the Nishikawa cell face gradient method. The governing equations were solved implicitly using the SGS defect correction scheme described in Ref. [4], with local time stepping and the CFL number linearly varied from 0.1 to 250 over time steps 1 to 500. Convergence was achieved by "freezing" the gradient limiter after 600 time steps to prevent convergence stalling due to limiter "ringing". The computations were stopped when the residual L_2 norm had dropped to machine zero. The 2-D geometry was discretized to form a 3-D computational domain using the Pointwise® unstructured grid generator. The resulting grid consisted of triangular and quadrilateral 2-D cells, as shown in Fig. 18, extruded in the Z-direction to form a 3-D grid of 15,781 prismatic and 8,168 hexahedral cells for a total of 23,949 cells. The boundary conditions were: 1) reflection of all variables at the min. and max. Z-direction boundary cell faces (Symmetry Boundary), 2) specification of all variables on the min. X-direction boundary cell faces (Inflow Boundary), 3) 1st-order extrapolation of all variables at the max. X and Y-direction boundary cell faces (Outflow Boundary) and 4) isothermal no-slip wall-matching construction of all variables on the min. Y-direction wall boundary cell faces (No-slip Isothermal Wall). The computations were performed using parallel processing on 6 partitions. Results are presented for computations without use of the pressure limiter and with and without eliminating limiting when expansion is present. Figure 19 presents Mach contours for three computations; 1) without the pressure limiter, 2) with the pressure limiter and 3) with the pressure limiter constrained to compression only. This figure clearly demonstrates the detrimental effects of using the pressure limiter and how the compression only limiter mitigates some of these detrimental effects. It should also be noted that the effect of the dissipation added by the compression only limiter can also be seen in Fig. 19 as a reduction in the length of the separation bubble downstream of the backward facing step.

E. Hypersonic Turbulent Flow Over a Notional Scramjet Fuel injector Using Tetrahedral, Prismatic, Pyramidal and Hexahedral Cells.

The third numerical experiment was conducted by computing hypersonic, thermally prefect, chemically frozen, turbulent flow over an isolated notional scramjet fuel injector strut. The freestream conditions were: P_{ref}= 50,662.5 Pa, T_{ref}= 1,297.7 K, and Mach number, M_{ref}= 6.35. A thermally perfect mixture two species, O2 and N2, having mass fractions of 0.767 and 0.233 respectively was used to simulate the test gas, which at the given conditions yields a unit Reynolds number of Re_{ref}= 1.1869×10^7/m. The wall surface was treated as a no-slip, adiabatic wall, using a turbulent wall matching boundary conditions [38]. The Menter Baseline two-equation turbulence model [40] was used to compute the Reynolds stresses and Reynolds heat flux (Pr_t=0.9), and the turbulence model production term was based on the magnitude of the vorticity. The inviscid fluxes were computed using the LDFSS scheme with the higher-order cell-face states reconstructed using the LP-U-MUSCL, $\kappa = 1/3$, approach with the face-averaged gradients limited using the gradient limiter described by Eqs. [35-40] where the actual limiter function used was the vanAlbada function. The viscous fluxes were computed using the Nishikawa cell-face gradient method. Convergence was achieved by "freezing" the gradient limiter after 1500 time steps to prevent convergence stalling due to limiter "ringing". The governing equations were solved implicitly using the SGS defect correction scheme, with local time stepping and the CFL number linearly varied from 0.1 to 100 over time steps 1 to 250 for a total of 5000 iterations. The strut geometry was discretized to form a 3-D computational domain using the Pointwise® unstructured grid generator as shown in Fig. 19. The resulting grid consisted of a combination of quadrilaterals and triangles on the boundaries, as shown in Figs. 20 and 21. All boundary surfaces were extruded normal to the surface to form layers of hexahedral and prismatic cells. These hexahedral and prismatic layers were then transitioned to tetrahedral cells via a layer of pryamidal cells to form a 3-D grid consisting of 484,579 hexahedral, 23,223 prismatic, 249,176 pyramidal and 484,579 tetrahedral cells for a total of 2,050,581 cells. The boundary conditions, as shown in Fig. 20 were: 1) reflection of all variables at the max. Y-direction boundary cell faces (Freestream Boundary), 2) specification of all variables on the min. X-direction boundary cell faces (Inflow Boundary), 3) 1st-order extrapolation of all variables at the max. X-direction boundary cell faces (Outflow Boundary) and 4) adiabatic wall-matching on the min. Y-direction and strut surface wall boundary cell faces (No-slip Adiabtic Wall Boundary). The computations were performed using parallel processing on 24 partitions. Figure 22 presents a more detailed view of the outflow boundary grid where a colliding front is pointed out. This detail results from the convergent normals of the bottom wall and strut side wall boundaries. The grid quality at the outflow is not too concerning. However, if one plots a constant X-direction slice upstream of the outflow boundary, as shown in Fig. 23, the cells can be seen to be highly sewed and flattened. This area of the grid contains cells with included angles of leass than 0.04 degrees and as such is considered a problematic grid and is why this grid was chosen as a test case for the F-ANG+ scheme. In addition, the use of wall functions for this case, causes the F-ANG+ scheme to use the F-ANG+*fn* and the F-ANG-*nn* stencils. This is because wall function stencils do not include wall face values and on some grids can result in stencils that are not well posed. Figure 24 presents a composite contour plot where the wall pressure contours are plotted on the adiabatic wall faces and slices reveal the outflow boundary, strut midline XY plane and constant XZ plane Mach contours showing the solution to be well behaved. Finally, the convergence history of the strut computation is presented in Fig. 25 where the residual can be seen to have converged in a reasonably well behaved manner approximately six orders of magnitude from its largest value.

IV. Summary and Conclusions

The development of novel gradient construction approaches have been pursued due to a near-term desire to reduce, in terms of computational effort and storage, the cost of computing weighted least-squares gradients (WLSQ) on general unstructured grids. We were further motivated by a long term need to improve the fidelity and robustness of the cell centered, finite-volume, unstructured grid method on the highly skewed tetrahedral grids that can be produced by current tetrahedral unstructured grid adaptation algorithms. In particular, a method for computing WLSQ gradients at the grid nodes, and the related 2-D face-averaged nodal-gradient (F-ANG+*fn*) approach of Nishikawa and White was extended to 3-D and a further augmented (F-ANG+*nn*) approach was developed to allow for stencil expansion when near boundary stencils become difficult to assemble. This resulted in the development of a novel 3-D approach (F-ANG+) for computing WLSQ gradients at the nodes, averaging of those nodal gradients to the cell faces, and the use of the averaged nodal gradients in constructing the inviscid and viscous fluxes in a 2nd-order accurate, cell-centered, finite-volume unstructured mixed-grid-based solver. A quadratic least squares approach to computing the WLSQ gradient was described and a new approach to constructing the gradient limiters on the faces that produces a limiter that is consistent with the LP-U-MUSCL scheme for all values of κ was also described. Finally, an improvement to the pressure limiter of Gnoffo was described that constrains the limiters action to compressing flow. The accuracy of the F-ANG+ scheme was explored via the laminar hypersonic flow of thermally-perfect air over a flat plate. This was accomplished by performing a 2-D structured grid resolution study using the VULCAN-CFD structured grid solver to establish a "reference" grid-resolved wall heat transfer distribution. A 3-D grid resolution study using the F-ANG+ approach on a series of regular tetrahedral grids was performed and compared against the 2-D "reference" solution. The conventional, 3-D, node-neighbor cell-centered gradient approach (*nn*-CCG) was also compared against this reference solution and the F-ANG+ solution on one of the regular tetrahedral grids. For this tetrahedral grid, the 3-D F-ANG+ nodal gradient approach was found to be the most accurate and to reduce the cost of computing the WLSQ gradients by a factor of 8.9 compared to the 3-D *nn*-CCG approach. In addition, the sketch-to-solution grid adaptation approach was used to explore the behavior of F-ANG+ on extremely skewed tetrahedral grids using the weighted linear least squares scheme (WLLSQ) and the weighted quadratic least squares scheme (WQLSQ) to compute the gradients. Both schemes were found to produce excellent results with the quadratic scheme results being slightly less oscillatory than the linear scheme. Turbulent hypersonic flow over a backward facing step was used to demonstrate the behavior of the compression constrained Gnoffo pressure limiter. Finally, turbulent hypersonic flow over a notional scramjet combustor fuel injector strut was computed to demonstrate that the F-ANG+ scheme is stable in 3-D on problematic grids for advection and diffusion on grids containing hexahedral, prismatic, pyramidal and tetrahedral cells.

Acknowledgments

This work was supported by the Hypersonic Technology Project, through the Hypersonic Airbreathing Propulsion Branch of the NASA Langley Research Center. In addition, we would like to thank Dr. Boris Diskin, of the National Institute of Aerospace, and Dr. Kyle Thompson of the Aerothermodynamic branch for their many helpful suggestions.

Figures

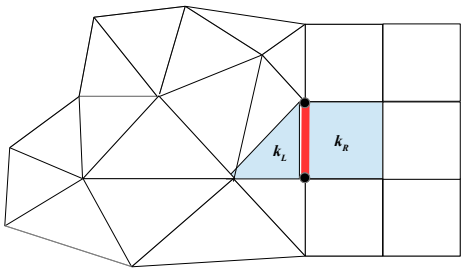
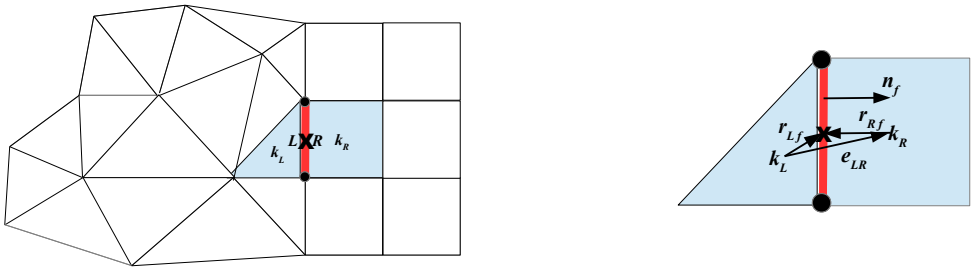
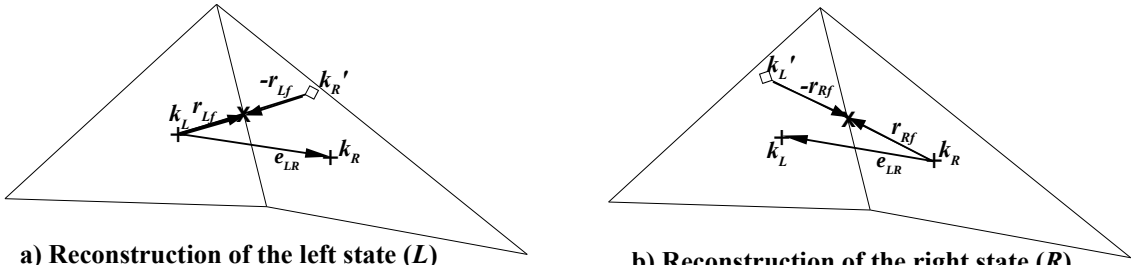


Fig. 1. 2-D hybrid-grid control-volume interface between the triangular cell, k_L, and the quadrilateral cell, k_R.



a) Reconstruction to the cell face centroid **b) Reconstruction vectors**

Fig. 2., 2-D reconstruction of the *L* and *R* states at the hybrid cell face centroid, f_c, x, for the inviscid and viscous fluxes.



a) Reconstruction of the left state (*L*) using k_L, k_R and k'_R

b) Reconstruction of the right state (*R*) using k_L, k'_L and k_R

Figure 3. Linearity preserving U-MUSCL reconstruction of the left and right states.

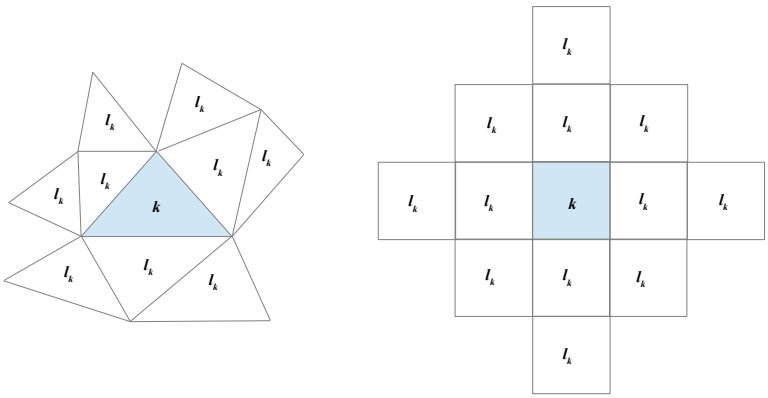


Fig. 4. The 2-D *fn2*-CCG WLSQ stencil, $\{l_k\}$, for cell, *k* (blue shaded area), on representative triangular and quadrilateral grids.

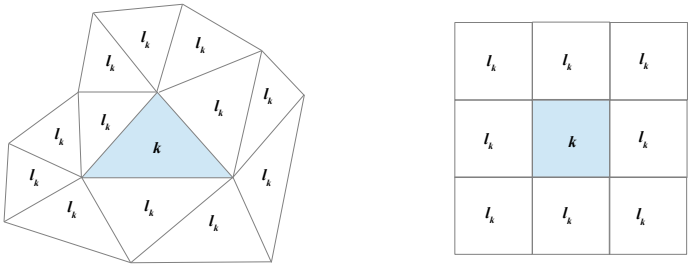


Fig. 5. The 2-D *nn*-CCG WLSQ stencil, $\{l_k\}$, cell, *k* (blue shaded area), on representative triangular and quadrilateral grids.

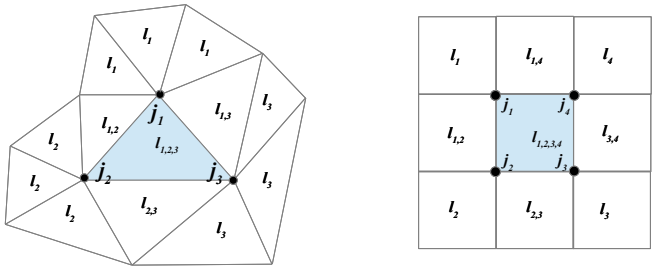
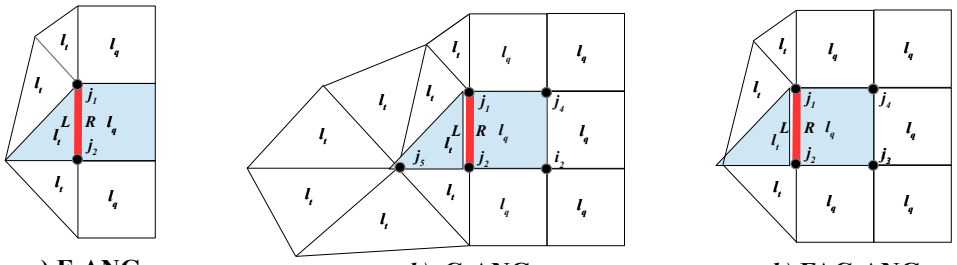
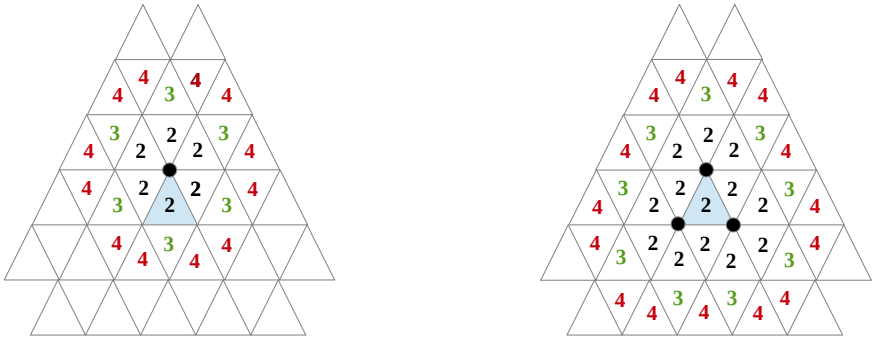


Fig. 6.The 2-D stencils $\{l_i\}$, for computing the WLSQ gradients at the nodes $j=1, 2, \ldots, N_{cell(1)}^{nodes}$ for cell, *k* (blue shaded area), on representative triangular and quadrilateral grids.



a) F-ANG **b) C-ANG** **b) FAC-ANG**

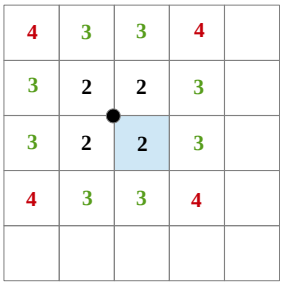
Fig. 7 The 2-D stencils $\{l_i\}$, for computing the WLSQ gradients at the nodes, $i_{1\text{-}N}$, for control volume, *k* (blue shaded area), on representative triangular and quadrilateral grids.



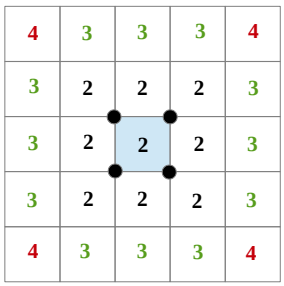
a) Candidate node-centered gradient stencils, with (2) and without (3 & 4) augmentation

b) Candidate residual stencils, with (2) and without (3 & 4) augmentation

Fig. 8. Candidate stencil augmentations of a node-centered gradient on a grid of triangles.

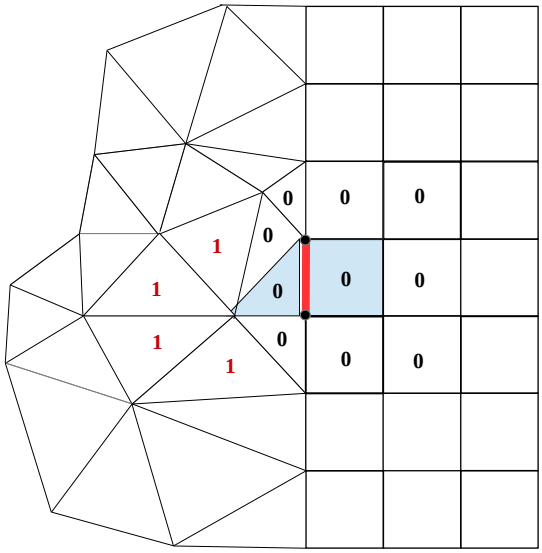


a) Candidate node-centered gradient stencils, With (2, 3 & 4) and without (2) augmentation

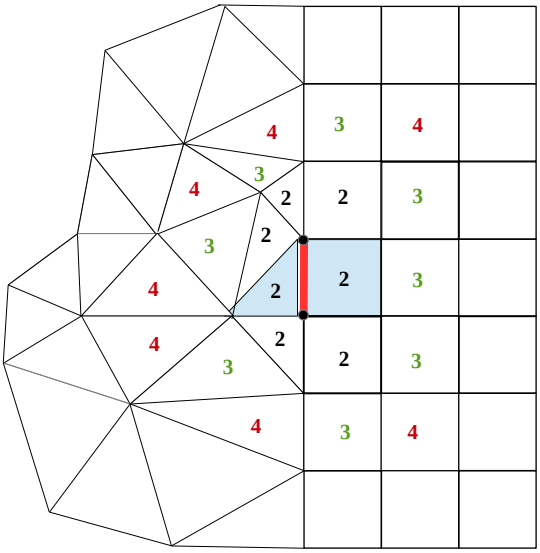


b) Candidate residual stencils, with (2, 3 & 4) and without (2) augmentation

Fig. 9. Candidate stencil augmentations of a node-centered gradient on a grid of quadrilaterals.

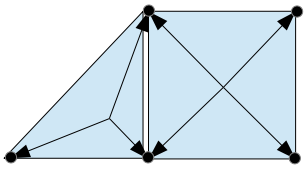


a) The cells labeled 0 define the FAC-ANG face stencil, the cells labeled 0 and 1 define the C-ANG face stencil

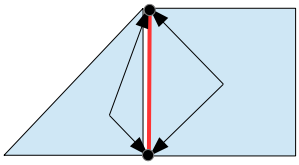


b) The cells labeled 2 and 3 define the F-ANG+fn face stencil, the cells labeled 2, 3 and 4 define the F-ANG+nn face stencil

Fig. 10. A comparison of the FAC-ANG face nodal gradient stencils with F-ANG+*fn* and F-ANG+*nn* face nodal gradient stencil on a hybrid grid of triangles and quadrilaterals.



a) Reconstruction to the all the nodes of each cell inside of a loop over cells



b) Reconstruction to all the nodes of each face for the cells that share the face inside of a loop over faces

Fig. 11. A comparison of cell MLP gradient limiter coefficient construction using a cell-based and a face-based approach.

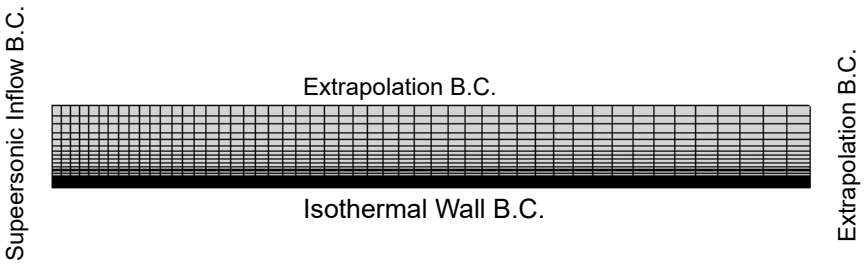


Fig. 12. Mach 6, 2-D, laminar flat plate, 2-D 101x77 structured grid with every other grid line removed.

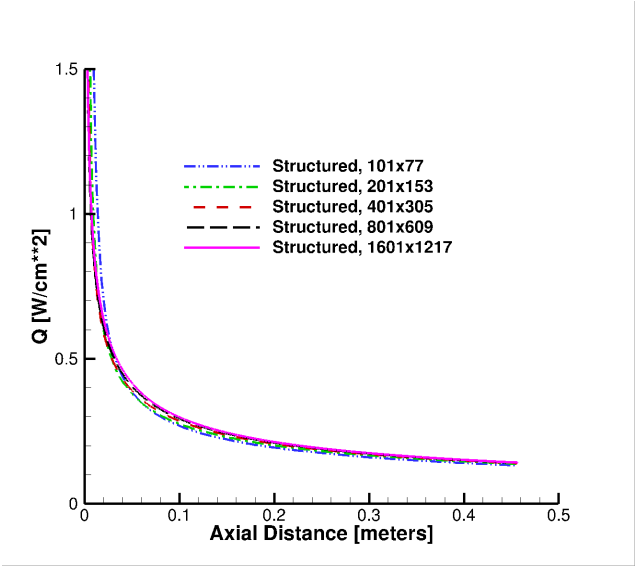


Fig. 13. Mach 6, 2-D, laminar flat plate, 2-D structured grid wall heat transfer grid resolution study.

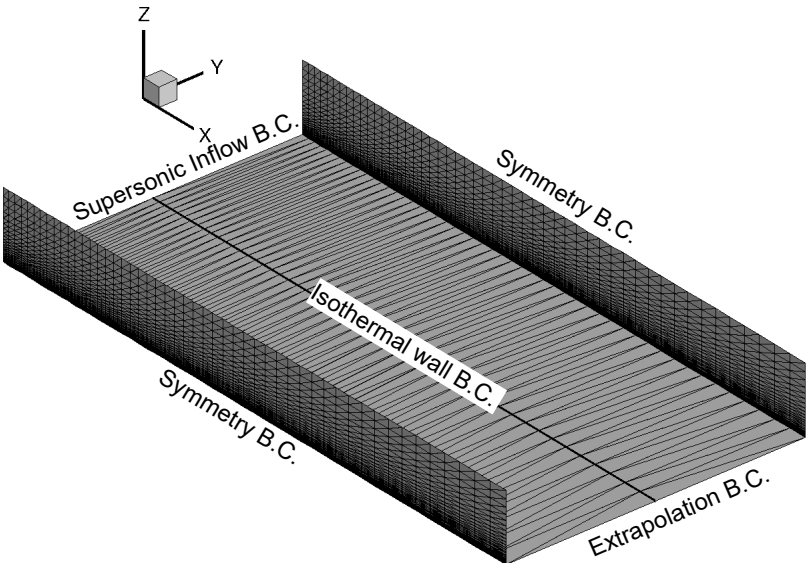
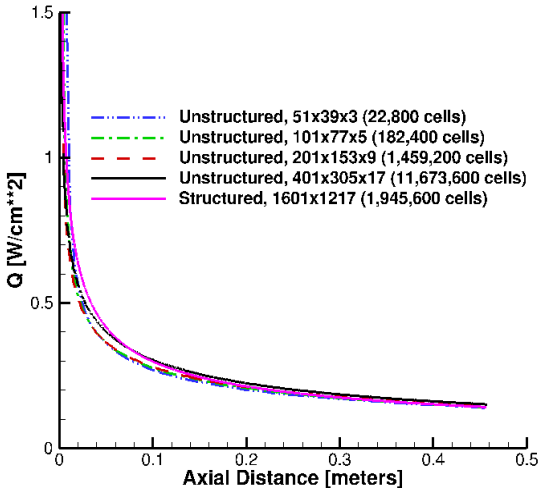
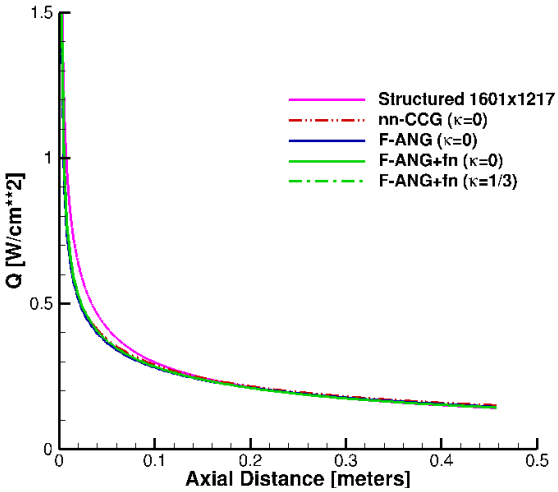


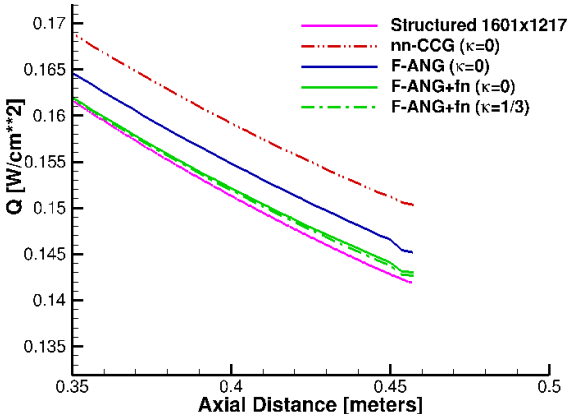
Fig 14. Mach 6, 2-D, laminar flat plate, 3-D 51x39x3 node tetrahedral cell grid based on a 51x39 node 2-D structured grid.



a) Unstructured wall heat transfer grid resolution study Using the F-ANG+*fn* scheme.



b) Comparison of the *nn*-CCG, F-ANG and F-ANG+*fn* schemes using the 201x153x9 grid.



c) A magnified view near the plate trailing edge comparing the *nn*-CCG, F-ANG and F-ANG+*fn* schemes using the 201x153x9 grid.

Fig. 15. Mach 6.0, 2-D laminar flat plate comparison of heat transfer on structured and unstructured tetrahedral grids for solution using *nn*-CCG, F-ANG and FANG+*fn* WLLSQ schemes.

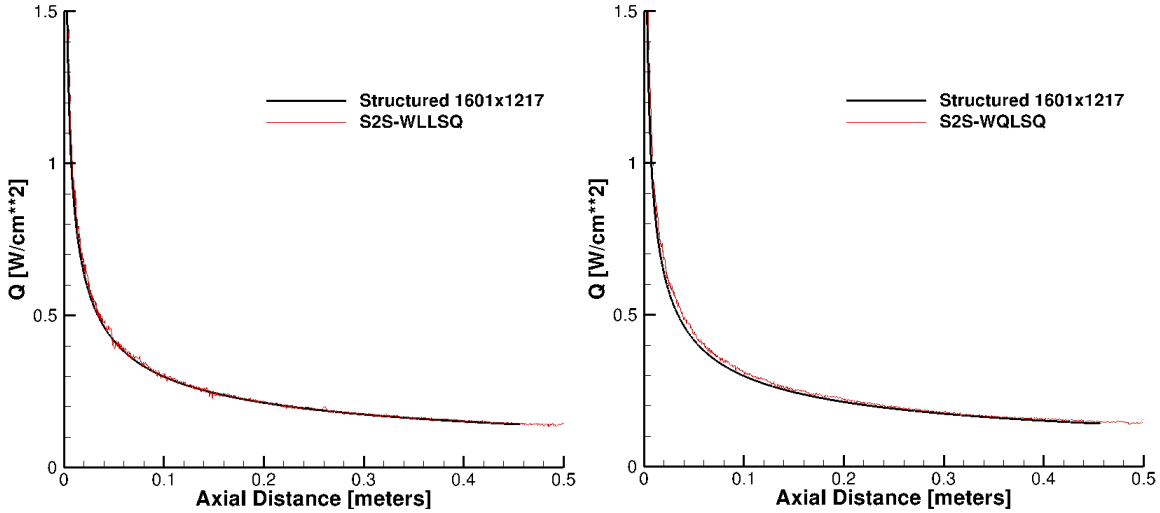
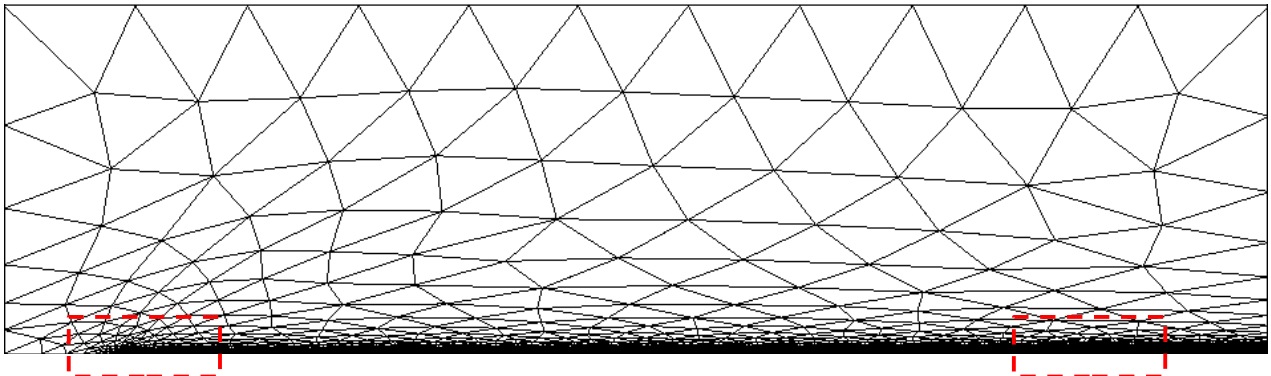
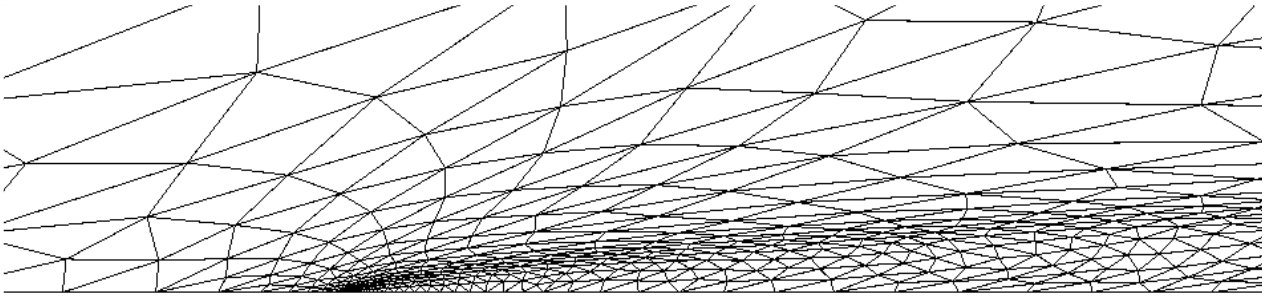


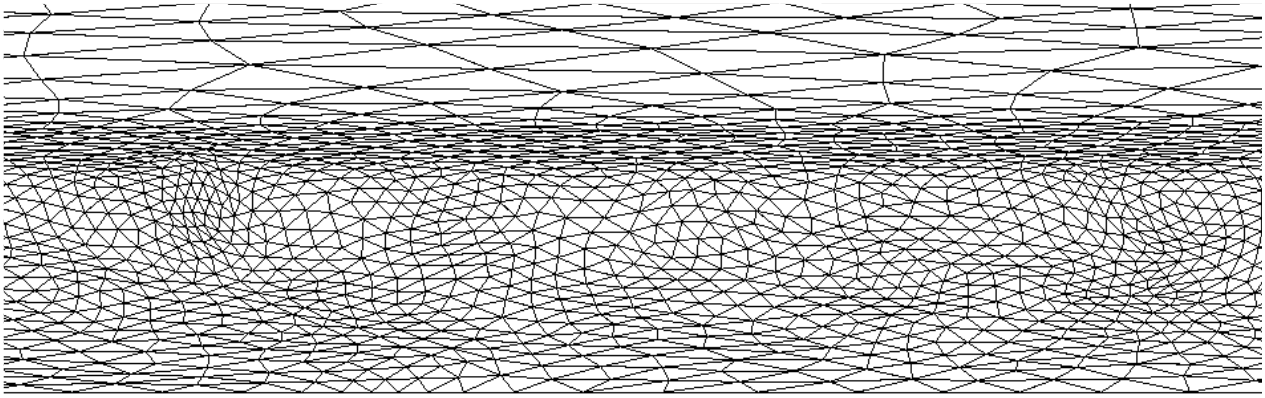
Fig. 16. Mach 6.0, 2-D laminar flat plate comparison of heat transfer on structured and adapted unstructured tetrahedral grids for solution using the FANG+*fn* approach linear and quadratic WLSQ schemes.



a) Adapted laminar flat plate boundary layer grid.



b) Detailed view of the adapted laminar boundary layer grid near the flat plate leading edge.



c) Detailed view of the adapted laminar boundary layer grid near the flat plate trailing edge.

Figure 17. Mach 6 laminar flat plate *refine* adapted grid using the sketch-to-solution workflow after 29 grids using total enthalpy Hessian as the adaptation metric.

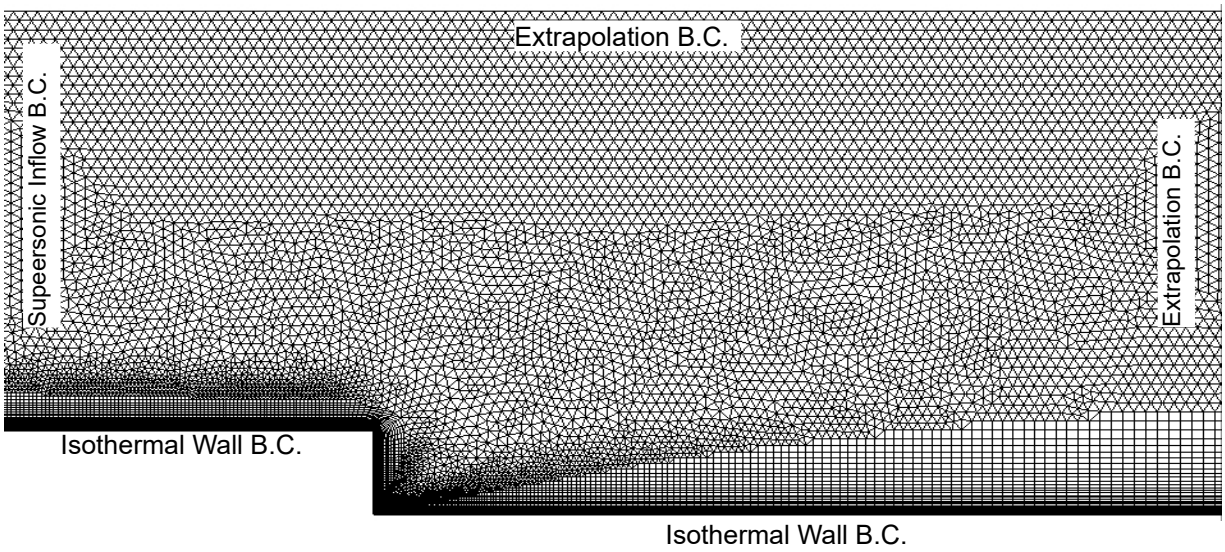


Fig. 18. Computational grid and boundary conditions for hypersonic flow over a 2-D backward facing step.

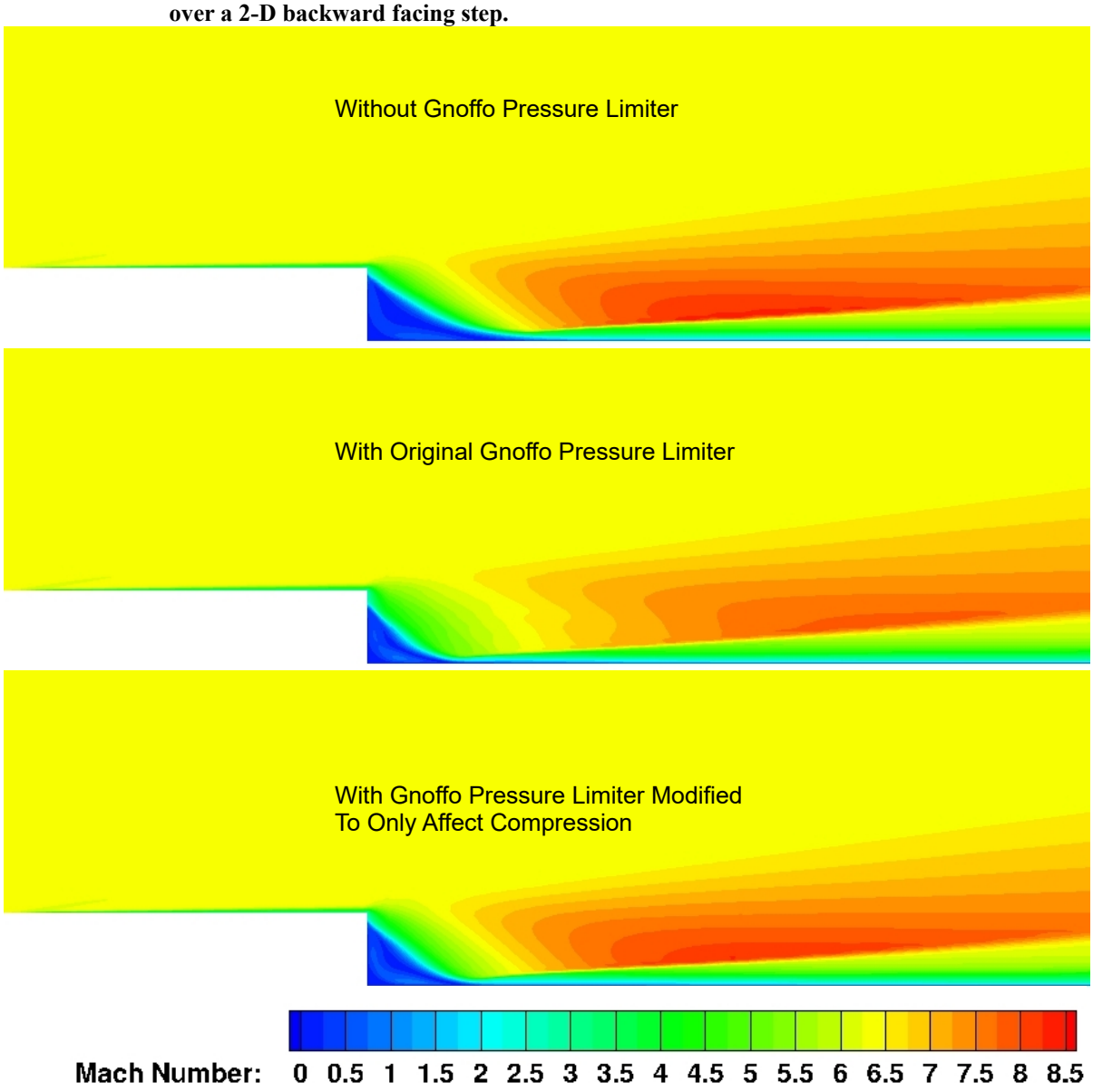


Fig. 19. Mach contours for computations of a hypersonic flow over a 2-D backward facing step without a pressure limiter, with a pressure limiter and with a compression only limiter.

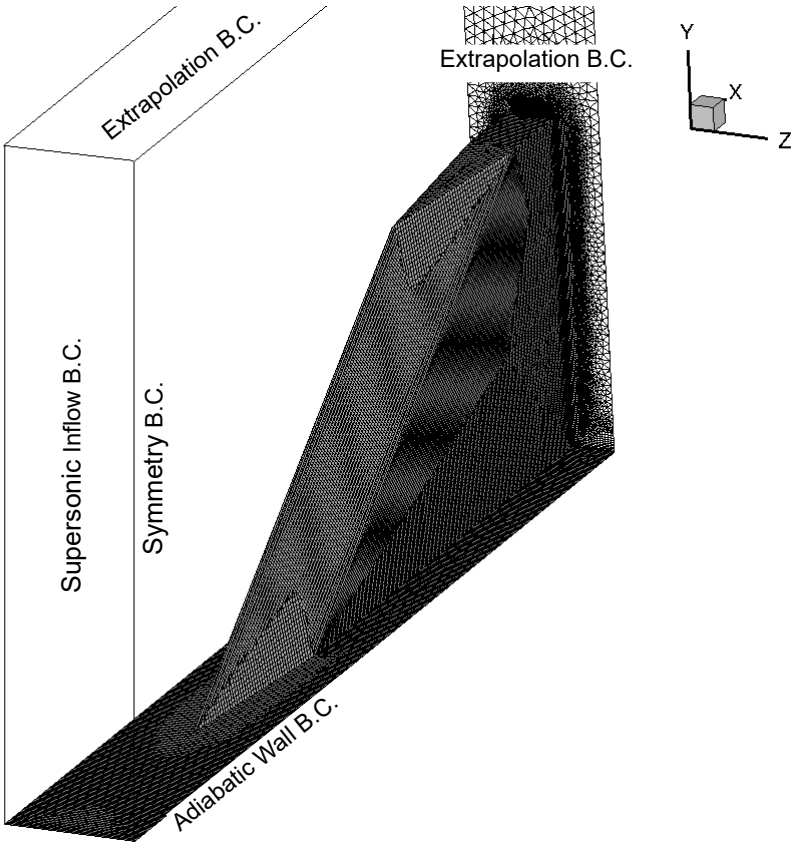


Fig. 20. Computational domain for computing hypersonic turbulent flow over a notional fuel injector strut.

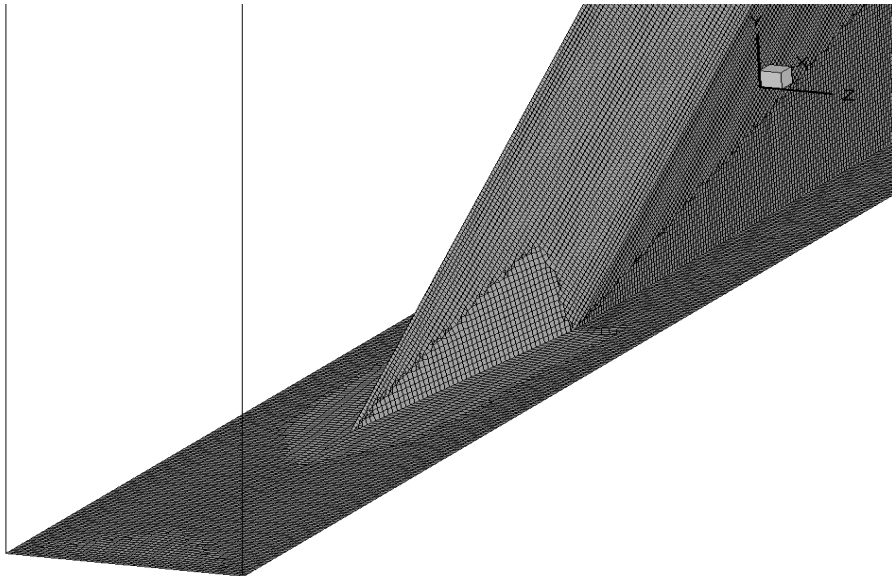


Fig. 21. Strut leading edge detail of adiabatic wall surface grid constructed using hexes and triangles.

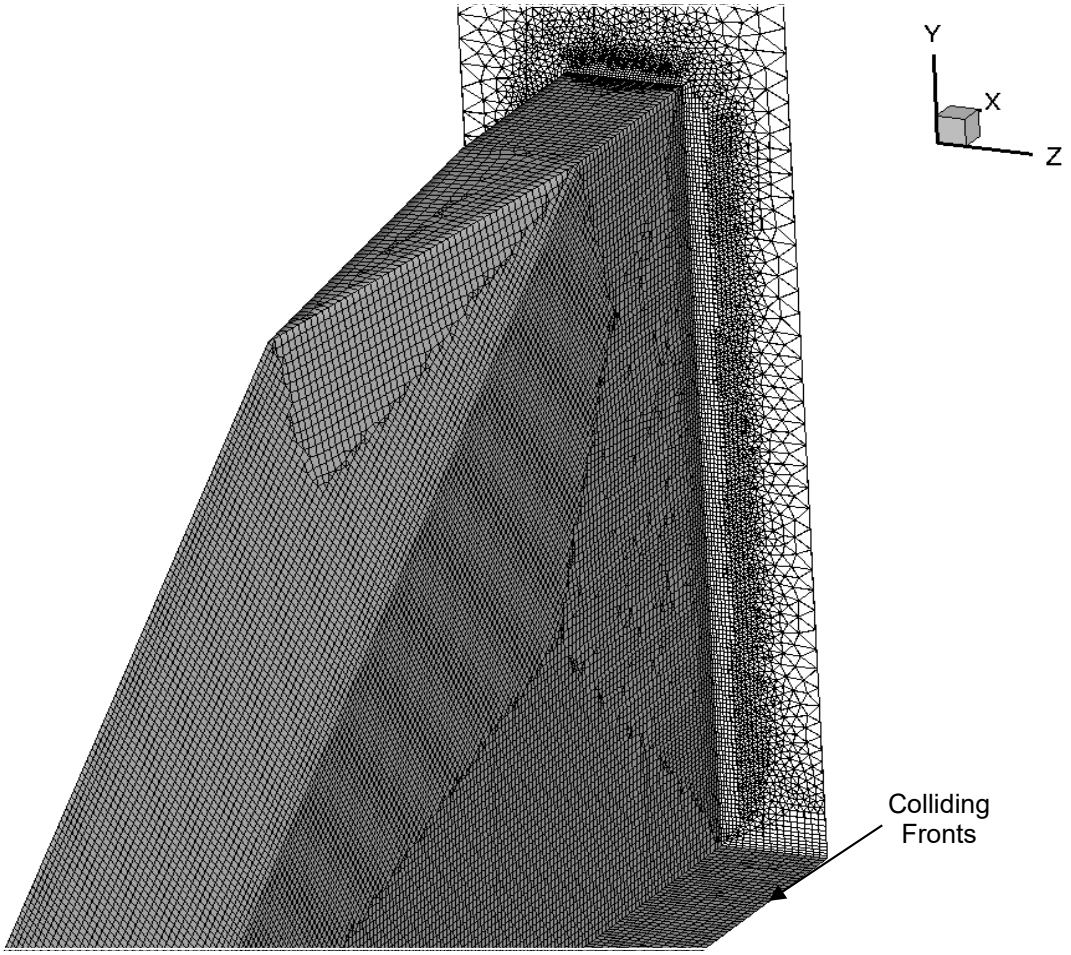


Fig. 22. Strut top and body adiabatic wall and outflow boundary details of surfaces grids constructed using hexes and triangles.

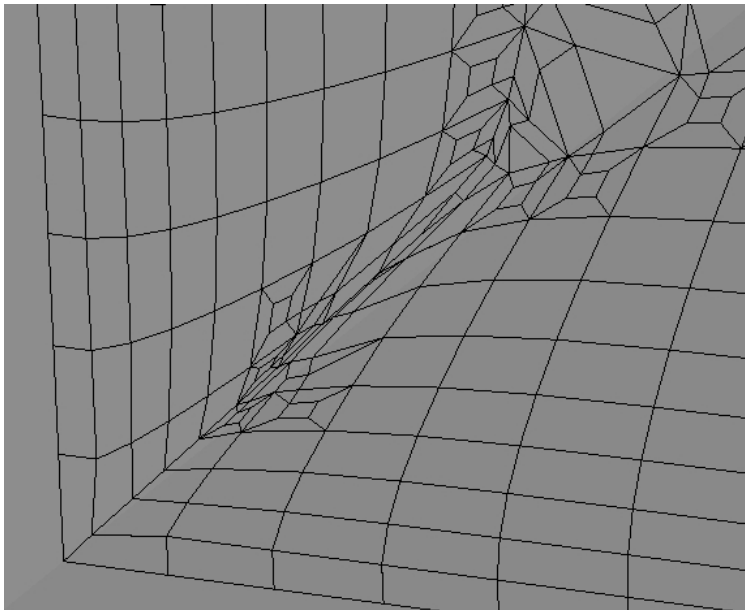


Fig. 23. Colliding front detail of a grid constant X slice where cells have very small included angles.

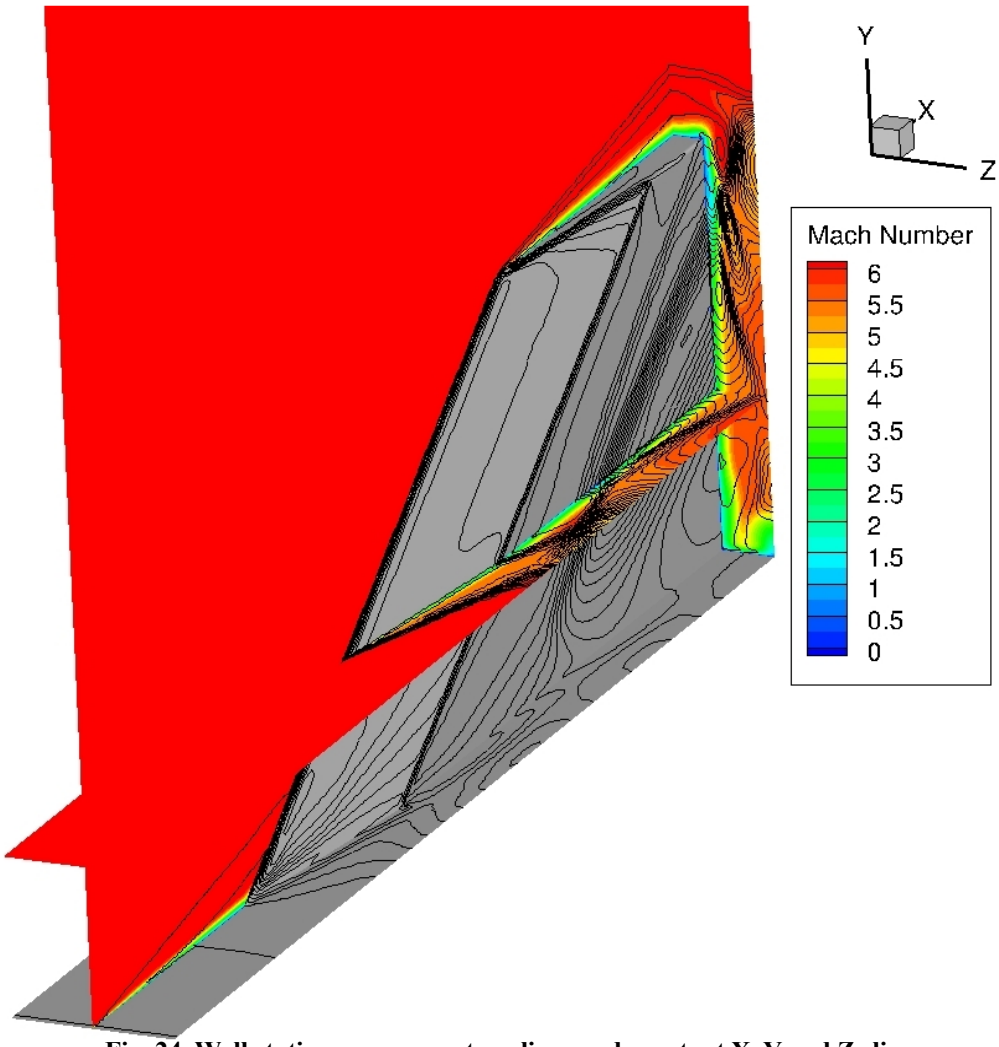


Fig. 24. Wall static pressure contour lines and constant X, Y and Z slices of Mach No. flood and line contours.

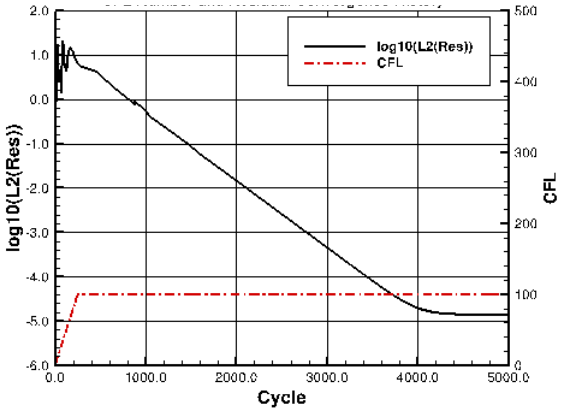


Fig. 25. Convergence behavior of the notional hypersonic strut case using the F-ANG+ approach.

References

1. Kleb, W. L., Park, M. A., Wood, W. A., Bibb, K. L., Thompson, K. B., and Gomez, R. J., "Sketch-to-Solution: An Exploration of Viscous CFD with Automatic Grids," AIAA Paper 2019-2948, June, 2019. doi:10.2514/6.2019-2948
2. Park, M.A., Kleb, B. Jones, W.T., Krakos, J.A., Michal, T. Loseille, A, Haimes, R. and Dannenhoffer, J.F.III, "Geometry Modeling for Unstructured Mesh Adaptation," AIAA Paper 2019-2946, June, 2019. doi:10.2514/6.2019-2946
3. O'Connell, M.D.,White, J.A. and Thompson, K.B., "Towards an Automated Unstructured Grid Adaptation Workflow with VULCAN," AIAA Paper 2021-2701, Aug. 2021. doi:10.2514/6.2021-2701
4. White, J. A., Baurle, R. A., Passe, B. J., Spiegel, S. C. and Nishikawa, H., "Geometrically Flexible and Efficient Flow Analysis of High Speed Vehicles Via Domain Decomposition, Part 1, Unstructured-grid Solver for High Speed Flows," JANNAF 48th CS / 36th APS / 36th EPSS / 30th PSHS Joint Subcommittee / Programmatic and Industrial Base Meeting, Newport News, VA, Dec., 2017.
5. Nishikawa, H., "Efficient Gradient Stencils for Robust Implicit Finite-Volume Solver Convergence on Distorted Grids," *J. of Comput. Phys.*, Vol. 386, 2019, pp. 486-501. doi:10.1016/j.jcp.2019.02.026
6. White, J. A., Nishikawa, H., and Baurle, R. A., "Weighted Least-squares Cell-Average Gradient Construction Methods For The VULCAN-CFD Second-Order Accurate Unstructured-Grid Cell-Centered Finite-Volume Solver", AIAA Paper 2019-0127, January 2019. doi:10.2514/6.2019-0127
7. White, J. A., Baurle, R. A. and Nishikawa, H., "Efficient and Robust Weighted Least-squares Cell-Average Gradient Construction Methods for the Simulation of Scramjet Flows," JANNAF 49th CS / 37th APS / 37th EPSS / 31st PSHS Joint Subcommittee, Dayton, OH, June 2019.
8. White, J.A., Nishikawa, H. and Baurle, R.A., "A 3-D Nodal-Averaged Gradient Approach for Unstructured-Grid Cell-Centered Finite-Volume Methods for Application to Turbulent Hypersonic Flow," AIAA Paper 2020-0652, Jan. 2020. doi:10.2514/6.2020-0652.
9. Nishikawan, H. and White, J. A., "An Efficient Cell-Centered Finite-Volume Method with Face-Averaged Nodal-Gradients for Triangular Grids," J. Comput. Phys.,Vol. 411, 2020. doi:10.1016/j.jcp.2020.109423
10. Nishikawa, H. and White, J. A., "Face-Averaged Nodal-Gradient Approach to Cell-Centered Finite-Volume Method on Triangular Grids,", AIAA Paper 2019-3636, June 2019. doi:10.2514/6.2019-3636
11. Nishikawa, H. and White , J.A., "A Simplified FANG Cell-Centered Finite-Volume Method and Comparison with Other Methods for Trouble-Prone Grids," To be published, AIAA Aviation Forum, Aug. 2021.
12. Park, J. S. and Kim, C., "Multi-dimensional Limiting Process for Finite Volume Methods on Unstructured Grids," *Computers & Fluids*, Vol. 65, Elsevier Ltd, 2012, pp. 8–24. doi:10.1016/j.compfluid.2012.04.015
13. Nishikawa, H., "On The Loss And Recovery Of Second-order Accuracy With U-MUSCL," *J. of Comput. Phys.*, Vol. 417, 2020, doi:10.1016/j.jcp.2020.109600
14. Burg, C. O. E., "Higher-Order Variable Extrapolation for Unstructured Finite Volume RANS Flow Solvers," AIAA Paper 2005-4999, June 2005. doi:10.2514/6.2005-4999
15. Schwoppe, A. and Diskin, B., "Accuracy of the Cell-Centered Grid Metric in the DLR TAU-Code," *New Results in Numerical and Experimental Fluid Mechanics VIII. Notes on Numerical Fluid Mechanics and Multidisciplinary Design*, Vol. 121, 2013, Springer Berlin Heidelberg, pp. 429-437.
16. Sozer, E., Brehm, C. and Kiris, C. C., "Gradient Calculation Methods on Arbitrary Polyhedral Unstructured Meshes for Cell-Centered CFD Solvers," AIAA Paper 2014-1440, January 2014. doi:10.2514/6.2014-1440
17. Diskin, B. and Thomas, J. L., "Comparison of Node-Centered and Cell-Centered Unstructured Finite-Volume Discetizations: Inviscid Fluxes,"*AIAA Journal*, Vol. 49, No. 4, pp .836-854. doi:10.2514/1.J050897
18. Haider, F., Croiselle, J.-P., and Courbet, B., "Stability Analysis of the Cell Centered Finite-volume MUSCL Method on Unstructured Grids," *Numerische Mathematik*, Vol. 113, 2009, Springer Berlin Heidelberg, pp. 555-600.
19. Zangeneh, R. and Ollivier-Gooch, C. F., "Reconstruction Map Stability Analysis for Cell Centered Finite Volume Methods on Unstructured Meshes", AIAA Paper 2017-0734, January 2017. doi:10.2514/6.2017-0734
20. Zhang, F., Liu, J., Chen, B., and Zhong, W., "A Nodal-Weighted-Least-Squares Gradient Reconstruction for Cell-Centered Finite Volume Method," Unpublished, 2015.
21. Zhang, F., "A Vertex-Weighted-Least-Squares Gradient Reconstruction," arXiv:1702.04518 [physics.flu-dyn], 2017.
22. Zhang, F., "Research on Spatial Discretization Schemes for Finite Volume Method on Unstructured Grids," Ph.D. Thesis, Dalian University of Technology, 2017.
23. Frink, N. T., "Upwind Scheme for Solving the Euler Equations on Unstructured Tetrahedral Meshes," *AIAA Journal*, Vol., No. 1, January 1992, pp. 70-77. doi:10.2514/3.10884
24. Edwards, J. R., "A Low-Diffusion Flux-Splitting Scheme for Navier-Stokes Calculations," *Computers & Fluids,* Vol. 26, No. 6, 1997, pp. 635–659. doi:10.1016/S0045-7930(97)00014-5
25. Toro, E. F., Spruce, M., and Speares, W., "Restoration of the Contact Surface in the HLL-Riemann Solver," *Shock Waves,* Vol. 4, 1994, pp. 25–34.
26. Fromm, J. E., "A Method for Reducing Dispersion in Convective Difference Schemes," *Journal of Computational Physics*, Vol. 3, 1968, pp. 176–189.
27. Diskin, B., Thomas, J. L., Nielsen, E., Nishikawa, H. and White, J. A., "Comparison of Node-Centered and Cell-Centered Unstructured Finite Volume Discretizations: Viscous Fluxes," *AIAA Journal*, Vol. 48, No. 7, 2010, pp. 1326–1339. doi:10.2514/1.44940

28. Jalai, A., Sharbtdar, M. and Ollivier-Gooch C., "Accuracy Analysis of Unstructured Finite Volume Discretization Schemes For Diffusive Fluxes," *Computers & Fluids*, Vol. 101, 2014, pp. 220–232. doi:10.1016/j.compfluid.2014.06.008
29. Nishikawa, H., "Beyond Interface Gradient: A General Principle for Constructing Diffusion Schemes," AIAA Paper 2010-5093, June 2010. doi:10.2514/6.2010-5093
30. Strang, G., *Linear Algebra and Its Applications*, Academic Press, 2nd ed., 1980.
31. Nompelis, I., Drayna, T. and Candler, G., Development of a Hybrid Unstructured Implicit Solver for the Simulation of Reacting Flows Over Complex Geometries, AIAA Paper 2004-2227, June, 2004. doi:10.2514/6.2004-2227
32. Park,M.A., "Anisotropic output-based adaptation with tetrahedral cut cells for compressible flows", MIT Phd Dissertation, Sept., 2008. https://dspace.mit.edu/handle/1721.1/46363
33. Gnoffo, P.A. and White, J.A, "Computational Aerothermodynamic Simulation Issues on Unstructured Grids," AIAA-Paper 2004-2371, July, 2004. doi:10.2514/6.2004-2371
34. Wilcox, D. C., "Wall Matching, a Rational Alternative to Wall Functions," AIAA Paper 89-0611, January 1989.
35. Diskin, B. and Thomas, J. L., "Accuracy of Gradient Reconstruction on Grids with High Aspect Ratio," *NIA Report No. 2008-12* , 2008.
36. Chan, Y.K., Razzaqi, S. Smart, M.K. and Wise, D., "Freejet Testing of the 75%-scale HIFiRE 7 REST Scramjet Engine," AIAA Paper 2014-2931, June 2014. doi:10.2514/6.2014-2931
37. Wilcox, D. C., "Formulation of the k-omega Turbulence Model Revisited," *AIAA Journal*, Vol. 46, No. 11, 2008, pp. 2823-2838. doi:10.2514/6.2007-1408
38. Wilcox, D. C., *Turbulence Modeling for CFD*, 2nd ed., DCW Industries, Inc., La Canada, CA, 1998, pp.121-122.
39. van Leer, B., "Towards the Ultimate Conservative Difference Scheme. V. A Second-order Sequel to Godunov's Method," *J. of Comp. Physics,* Vol. 32, 1979, pp. 101–136.
40. Menter, F. R., "Two-Equation Eddy-Viscosity Turbulence Models for Engineering Applications", *AIAA Journal,* Vol. 32, No. 8, 1994, pp. 1598–160. doi:10.2514/3.12149